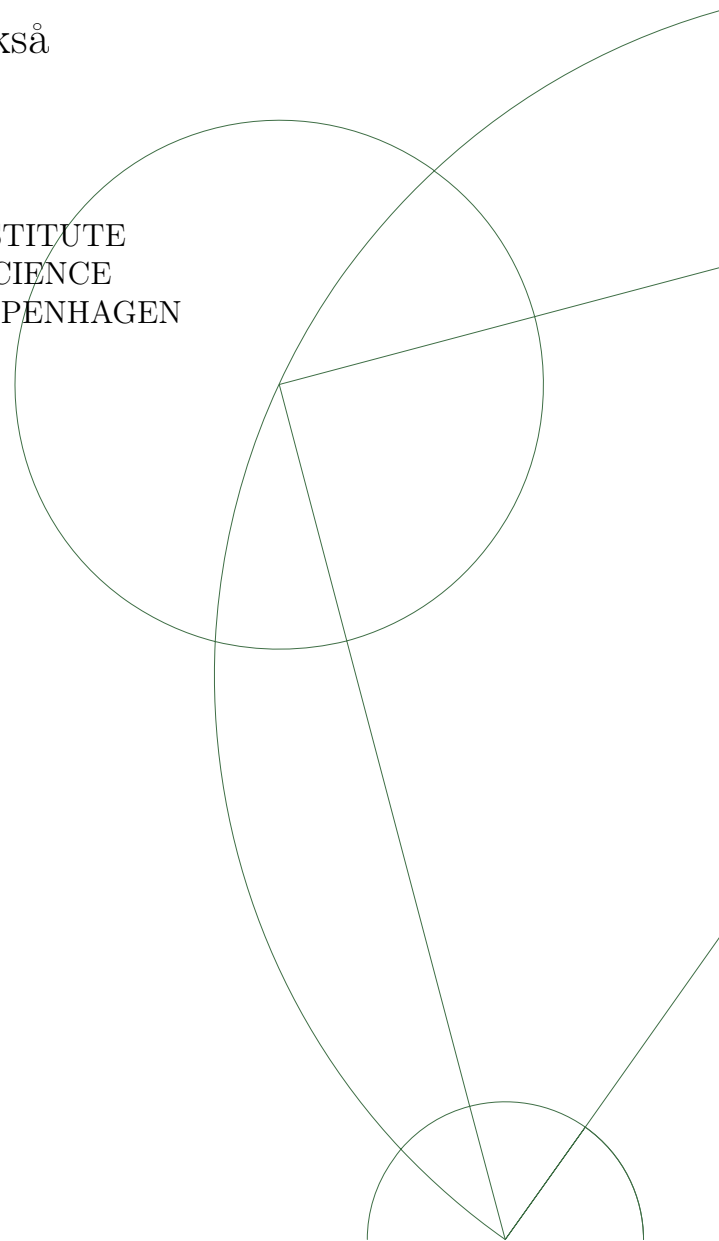MASTER THESIS
60 ETCS

Inertial resonance in the ocean mixed layer

Turid Lakså

NIELS BOHR INSTITUTE
FACULTY OF SCIENCE
UNIVERSITY OF COPENHAGEN

Supervisor:
Markus Jochum
Niels Bohr Institute
University of Copenhagen

11 September 2014

Abstract

Near-inertial waves affect the climate through mixing in the upper oceans and thereby the sea surface temperature. Changes in sea surface temperature lead to changes in the energy absorption in the oceans. Cold oceans contain less energy than warm oceans, hence cold oceans absorb more CO_2. It is therefore important to understand and parameterize near-inertial waves. To accurately simulate sea surface temperatures in climate models is important, since it can help produce more reliable estimates of CO_2 uptake in the future. The performance of the Climate Earth System Model (CESM) is examined by comparing winds, currents and temperatures with mooring data from the Pilot Research Moored Array in the Tropical Atlantic (PIRATA) project at two mooring sites located at 4°N 23°W and 12°N 23°W. The annual mean near-inertial velocity is determined using two different methods. One method determines the near-inertial variance of the near-inertial spectral band. The near-inertial velocity is found at 4°N 23°W to be 13.74 cm/s for the model and 12.14 cm/s for the observations, at 12°N 23°W the near-inertial velocities are found to be 11.06 cm/s for the model and 16.54 cm/s for the observations. The other method uses a Butterworth bandpass filter in the near-inertial frequency band, ranging between $0.7-1.3f_I$ with f_I as the local inertial frequency, filtering the current time series. The near-inertial velocities of this method are found to be 10.37 cm/s for the model and 9.97 cm/s for the observations at 4°N 23°W, and at 12°N 23°W they are found to be 8.54 cm/s for the model and 12.92 cm/s for the observations. A case study of Hurricane Helene examines the ocean response to a hurricane and how well it is resolved in the model compared to mooring data from the mooring site at 12°N 23°W. The observational temperature data show a clear indication of mixing during the passage of Hurricane Helene. This is recognized in the model as a deepening of the boundary layer depth, but this is not convincing since the deepening does not stand alone as a notable event. Looking over annual time series, it is found that, the model performs well since the estimates of the near-inertial velocities are consistent with previously published modeling and observational efforts. However, looking at a single storm event the model performs poorly in resolving the winds.

Resumé

Nær-inertielle bølger har en effekt på klimaet gennem blanding i det øvre ocean og dermed på overfladetemperaturen. Ændringer i overfladetemperaturen medfører ændringer i absorptionen af energi i oceanerne. Kolde oceaner kan indeholde mindre energi end varme oceaner, og dermed absorberer kolde oceaner mere CO_2. Det er derfor vigtigt at forstå og parameterisere nær-inertielle bølger. Det er vigtigt at kunne simulere overfladetemperaturer så præcist som muligt i klimamodeller, da det kan hjælpe til at producere mere pålidelige estimater af CO_2-optaget i fremtiden. Ydeevnen af Climate Earth System Model (CESM) bliver undersøgt ved at sammenligne vind- og strømhastighedsdata og temperaturer med observeret data fra to forankrede bøjer fra Pilot Research Moored Array in the Tropical Atlantic (PIRATA) projektet, beliggende på 4°N 23°W, og 12°N 23°W. Den nær-inertielle hastighed er fundet ved brug af to forskellige metoder. En metode bestemmer variansen af det nær-inertielle frekvensbånd. På 4°N 23°W er den nær-inertielle hastighed fundet til 13.74 cm/s for modellen og 12.14 cm/s for observationerne. På 12°N 23°W er den nær-inertielle hastighed fundet til 11.06 cm/s for modellen og 16.54 cm/s for observationerne. Den anden metode benytter et Butterworth båndpas filter i det nær-inertielle frekvensbånd, som spænder mellem $0.7 - 1.3 f_I$ med f_I som den lokale inertielle frekvens. Den nær-inertielle hastighed er med denne metode fundet til at være 10.37 cm/s for modellen og 9.97 cm/s for observationerne på 4°N 23°W og på 12°N 23°W er den fundet til 8.54 cm/s for modellen og 12.92 cm/s for observationerne. Der laves et case studie af Hurricane Helene for at undersøge, hvor godt den er bestemt af modellen, sammenholdt med observationer fra den forankrede bøje på 12°N 23°W. De observerede temperaturer viser en klar indikation af blanding under passagen af Hurricane Helene. Dette kan genkendes i modellen, ved at blandingslaget bliver dybere, men dette er ikke et overbevisende resultat, da det ikke er en enkeltstående markant begivenhed. En årlig tidsserie bliver repræsterer godt i modellen til forskel fra en enkelt stormbegivenhed, hvori vindene bliver simuleret ringe af modellen.

Contents

Abbreviations

ADCP	*Acoustic Doppler Current Profiler*
ATLAS	*Autonomous Temperature Line Acquisition System*
CCM	*Community Climate Model*
CCSM3	*Community Climate System Model version 3*
CCSM4	*Community Climate System Model version 4*
CESM	*Community Earth System Model*
CORE	*Coordinate Ocean Research Experiments*
FOCAL/SEQUAL	*Français−Océan−Climat Atlantique Equatorial/The Seasonal Response of the Equatorial Atlantic*
GCM	*Global Climate Model*
GIN Seas	*Greenland−Iceland−Norway Seas*
NCAR	*National Center for Atmospheric Research*
OCGM	*Ocean General Circulation Model*
PIRATA	*Pilot Research Moored Array in the Tropical Atlantic*
POP2	*Parallel Ocean Program version 2*
rms	*root-mean-square*
VOS	*Volunteer Observing Ships*

List of Figures

List of Tables

1 Introduction

The worlds oceans are large contributors to the climate on Earth and it is therefore very important to be able to predict them. The development of fully coupled climate models has therefore been a priority, and several attempts are made to improve the models. The improvement of the models could be an attempt on improving the air-sea fluxes determining the models.

Inertial waves are important for the climate, but they are typically not resolved in global climate models (GCMs), their importance is therefore not fully understood yet. Inertial waves are believed to play a primary role in the energy conversion of the oceans. They are proven (Dohan & Davis, 2011) to affect the deepening of the ocean mixed layer, and therefore they also affect the sea surface temperature of the ocean, and thereby how the ocean absorbs energy. Jochum et al. (2013) introduced a parameterization of the near-inertial wave mixing in the Community Climate System Model version 4 (CCSM4), in an attempt to improve the general understanding of the near-inertial waves.

Near-inertial waves affect the climate by their affect on the mixed layer and sea surface temperature. Near-inertial waves mix heat downwards, causing a decrease in the sea surface temperature. The decrease in sea surface temperature then increases the average net heat uptake in the oceans. The impact near-inertial waves have on the sea surface temperature also affect tropical precipitation and the large-scale atmospheric circulations. Even though the sea surface temperature changes in the tropics are small, they can lead to changes in the atmospheric large-scale Hadley and Walker cells (Jochum et al., 2013).

The changes in the sea surface temperature affects the uptake of energy in the oceans since colder oceans hold less energy than warm oceans, hence colder oceans absorb more CO_2, and hence the global warming can be slowed if the oceans are cooled. This is an important reason for the need to understand and parameterize near-inertial waves. It may help to more accurately simulate the observed sea surface temperature in climate models. This will help in the producing of more reliable estimates of CO_2 uptake over the coming century.

Near-inertial waves are a prominent feature of the ocean frequency spectra. A large amount of the total kinetic energy is contained inside the near-inertial frequency band (Alford et al., 2013). The work done by winds on near-inertial motions in the mixed layer is $0.3 - 1.4$ TW, which is a considerable amount of the 2 TW that are needed to maintain the abyssal stratification. Therefore it is believed that near-inertial waves also have a effect on the mixing in the deep oceans (Alford et al., 2012).

1

A large contributor to near-inertial wave activities in the mixed layer is the wind. The interaction between winds and near-inertial waves can enhance mixing in the mixed layer, which can contribute to a deepening of the mixed layer. The global variabilities in the oceans such as the El Niño Southern Oscillation are driven by heat in the mixed layer. These variabilities, and thereby the mixed layer, are essential to be able to predict.

The Ocean Storms Experiment [further reading, see Ocean Storms collection of papers: D'Asaro (1995a), Niieler & Paduan (1995), Large & Crawford (1995), Qi et al. (1995), Zervakis & Levine (1995), Levine & Zervakis (1995), D'Asaro et al. (1995), D'Asaro (1995b), D'Asaro (1995c), Large et al. (1995)] used a collection of drifting and moored data sets to examine the processes of air-sea interactions more closely.

In the Ocean Storms Experiment it is realized that inertial waves are a big part of the storm response. To understand the mixed layer evolution it is necessary to understand inertial waves (Large & Crawford, 1995). It is concluded that the inertial waves are important not only for the mixed layer, but also for the climate, and that the inertial waves are very poorly represented in the models (D'Asaro et al., 1995).

Dohan & Davis (2011) use data from the Ocean Storms Experiment to examine the response of the mixed layer to surface forcing during two storms of similar magnitude, but with very different responses in the mixed layer. They find that the mixed layer can be driven by different processes, and that they can give very different responses. One response is an enhancement of the eddy kinetic energy in the mixed layer caused by mixing that is driven by the wind stress at the surface, this is the classical response that causes a deepening of the mixed layer. Another response is that most of the wind is used in generating inertial oscillations, caused by resonant turning of the wind. Turbulent eddies contribute to the mixing, this response does not deepens the mixed layer, but the transition layer below (Dohan & Davis, 2011). This thesis is trying to follow on from this important study, trying to see whether the same kind of behavior, in developments of the mixed layer and the transition layer below, is seen during the passage of a storm.

A drifter buoy study by Elipot & Lumpkin (2008) finds the near-inertial velocities by a near-inertial variance method. A compromise between data availability and spectral resolution is found by dividing the oceans into latitudinal bands of 2.5°. Elipot et al. (2010) uses the same drifter buoy study with a higher spatial resolution of 1° to find the near-inertial velocities. The amplitude of near-inertial velocities is also found by Chaigneau et al. (2008), using satellite-tracked surface drifter data with a spatial resolution of 2°. This thesis uses mooring data and a forced simulation of a fully coupled model to find the near-inertial velocities using the near-inertial variance method and a Butterworth bandpass filter method. The results are compared with the results of Elipot & Lumpkin (2008), Elipot et al. (2010) and Chaigneau et al. (2008) as well as with the results from Jochum et al. (2013), who find the near-inertial velocities in a fully coupled model with a grid resolution of 1°.

Jochum et al. (2013) uses a coupled model to examine how well the near-inertial waves are represented in a fully coupled model. This thesis takes it a step further and looks at a forced simulation to see how well the near-inertial waves are represented. There are generally two issues that can be contributing to the failure of model representation of the

near-inertial waves; one is that the mixed layer physics could be wrong, and the other is that the forcing dataset could be wrong.

There has been an evolution in model understanding. The damped-slab layer model was used for several years before Plueddemann & Farrar (2006) compared it to a set of moorings and found, that the slab model performs very poorly when looking at the work done by winds on mixed layer inertial motions and at the inertial kinetic energy balance. Plueddemann & Farrar (2006) found that the observed kinetic energy balance is not properly reproduced by the slab model for strong resonant events. The time scale for strong inertially resonant wind forcing events are far to large in the slab model compared to the one of the moorings. Plueddemann & Farrar (2006) also compared the slab model and the moorings to another model, that includes shear instability mechanisms, which performed considerably better than the slab model for strong resonant events, indicating that the physical processes missing in the slab model is the shear-driven mixing at the mixed layer base. So Plueddemann & Farrar (2006) found, by comparing to moorings, that the slab model performs poorly. This thesis takes a forced simulation from a fully coupled model and compares with moorings to see if a fully coupled model has a better performance than the slab model.

1.1 Thesis Aims

The main motivation of this thesis is to understand the specific role of near inertial waves and the driving of vertical mixing. This is done by taking a Community Earth System Model (CESM) forced simulation and check how well it simulates near-inertial variability, by looking at annual time series at two different mooring sites (4°N 23°W and 12°N 23°W), finding the annual mean near-inertial velocity. A specific case study is done where it is examined which effect a hurricane has on the currents and the mixed layer depth.

This thesis will compare model data from the CESM forced simulation with observed mooring data from the Pilot Research Moored Array in the Tropical Atlantic (PIRATA) project. The compared data will be the wind stress, the currents and the sea surface temperature. The study will also look at the temperature with depth to see if there is a response to wind changes throughout the layers.

The thesis combines the theory and the model results and observations by comparing them. The theory and observations is used to examine the model performance and give suggestions to what could be wrong with the model.

Observations of Hurricane Helene are compared to the forced simulation in order to see how well hurricanes are resolved in the model. It is examined how well the wind and currents resolve the hurricane and what is happening in the mixed layer by looking at the temperatures in 12 different depths for the moorings and the boundary layer depth parameter in the model. It is investigated if oscillations of the temperatures in the depths are inertial oscillations by looking at frequency spectra. The frequency spectra of the wind stress and currents are compared to the model frequency spectra in order to examine the model performance. Near-inertial waves are a prominent feature of the ocean frequency

spectra, therefore the frequency spectra are particularly good to look at when it comes to examining model performance on near-inertial waves.

Another way of comparing the model and the moorings is calculating the near-inertial velocities. These are calculated using two different methods (the near-inertial variance method and the Butterworth bandpass filter method) at the two mooring sites, 4°N 23°W and 12°N 23°W, and the results are compared.

2 Scientific background

2.1 Dynamics of the ocean

This section will focus on the dynamics of the ocean, explaining about the mixed layer, the thermocline and the boundary layer depth. All of which are affected by the mixing that is created by the air-sea interaction.

2.1.1 The mixed layer

The mixed layer is a layer that is created when wind is blowing over the oceans. The wind stirs up the upper layers creating a thin mixed layer at the sea surface. Surface winds create turbulent mixing in the upper ocean, which leads to nearly uniform values of temperature and salinity in the upper 10-200 meters (Stewart, 2008). The mixed layer is the layer that is exposed to surface forcing and winds. It is in this layer most changes in the ocean take place.
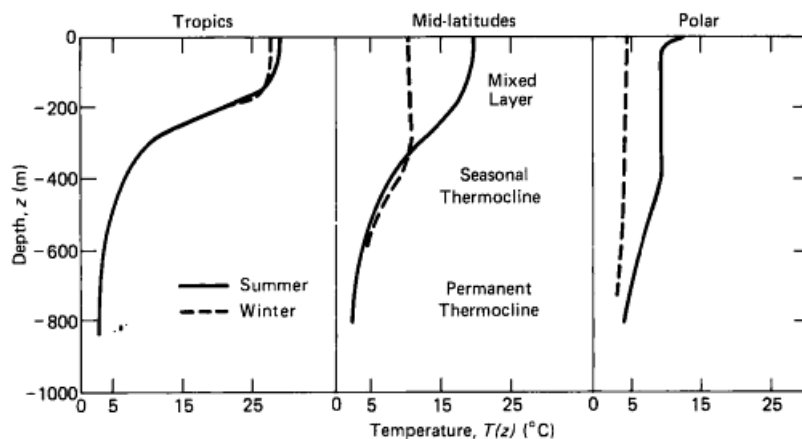
Figure 2.1: An idealized picture of how the temperature changes with depth in the top layers of the ocean, determining the mixed layer and the thermocline in the tropics (left), at midlatitudes (center) and in polar regions (right). Source: Apel (1988).

In the mixed layer the eddy diffusivity, K (also called the mixing coefficient), is much larger than it is in the thermocline below (Mellor, 1996). In figure 2.1, a temperature curve
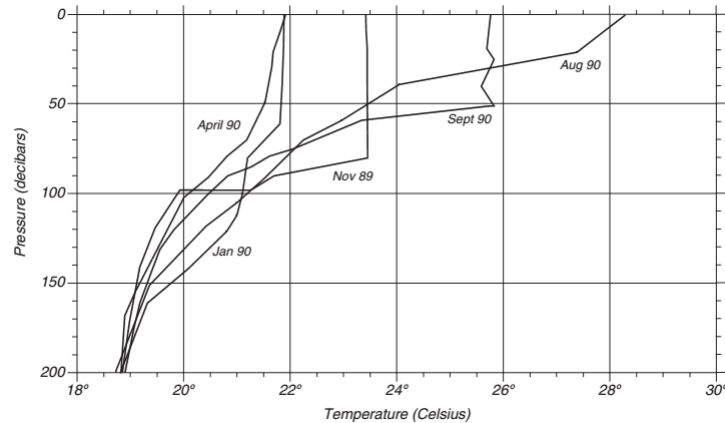
Figure 2.2: The depth of the mixed layer during the year. It is clear that the mixed layer is thinnest in the late summer, thickening during storm season due to mixing and reaching its maximum in the late winter where it has lost heat to the atmosphere. Source: Stewart (2008).

in the ocean is shown. The mixed layer ranges from the surface to the depth, where the values of temperature and hence density differ from those of the surface. The temperature at the bottom of the mixed layer should not be more than approximately $0.02 - 0.1$°C colder than at the surface (Stewart, 2008). The mixed layer is the warmest layer since it absorbs all its heat from the sun. The depth of the mixed layer varies with location, day and season. The thinnest mixed layer is found in the late summer, where the sun warms the water and the winds are weak. In the autumn, storms mix the heat down through the oceans, thickening the mixed layer. In the winter the oceans lose heat to the atmosphere and the mixed layer keeps thickening, reaching a maximum in the late winter (Stewart, 2008). This can be seen clearly in figure 2.2.

In the mixed layer components as temperature, salinity and density vary as a response to the exchange of heat and water with the atmosphere. Precipitation adds freshwater to the ocean and hence the salinity of the mixed layer is lowered. Evaporation removes freshwater from the ocean and hence the salinity of the mixed layer is increased (Wallace & Hobbs, 2006). On day to day and season to season basis the depth and temperature of the mixed layer varies in response to two processes: heating and cooling of surface waters due to heat fluxes through the surface and heat mixed downward by turbulence in the mixed layer (Stewart, 2008).

Mixing is a property that is highly affected by stratification. The stratification can be determined by the Richardson number, R_i:

$$R_i = \frac{-\frac{g \partial \tilde{\rho}}{\rho_0 \partial z}}{(\frac{\partial u}{\partial z})^2 + (\frac{\partial v}{\partial z})^2}. \tag{2.1}$$

The flow is determined by the size of the Richardson number. For $R_i < 0$ the flow will be unstable and the turbulent mixing will intensify. The mixing coefficient, K, increases

as the Richardson number becomes more negative. For $Ri = 0$ the flow will be neutral. Turbulent mixing is significant when the Richardson number lies in the range from zero to a critical value of the Richardson number, thought to be 0.2 to 0.25, such that $0 < R_i < R_{i,c}$. For $R_i > R_{i,c}$ the turbulent mixing will be very little and values of the mixing coefficient will be very small (Mellor, 1996).

Heat fluxes can create a strong stratification with a great contrast between the warm fresh water on top and dense colder water below. This strong stratification is often seen during the summer season. A strong stratification equals low potential energy and strong stability. The stronger stratification, the more energy is needed to mix the upper waters downward and lower waters upward. Thus the higher stratification, the more potential energy is required to induce mixing. It requires work to induce mixing on a stratified water column, so a mixed layer can be induced by a strong wind field at the surface (Knauss, 2005).

It can be crucial to predict changes in the mixed layer since they can have a large effects on the global climate.

2.1.2 The thermocline

The thermocline is the highly stratified transition layer that lies between the mixed layer and the weaker stratified deeper region. The beginning of the thermocline is in the tropics marked as an abrupt decrease in the water temperature with depth, as shown in figure 2.1 (Wallace & Hobbs, 2006).

2.1.3 The boundary layer depth

The boundary layer is the upper layer of the ocean determined by turbulent eddies. The boundary layer has often the same thickness as the mixed layer, this is because turbulent mixing is created by turbulent eddies, therefore the base of the layers will often be close to each other.

The boundary layer depth is defined as the depth range over which turbulent boundary layer eddies penetrate. It is calculated as the minimum depth at which the bulk Richardson number, Ri_b, exceeds the critical Richardson number $Ri_c = 0.3$ (Wallcraft et al., 2009).

The boundary layer depth, h_b, is derived from the bulk Richardson number

$$Ri_b = \frac{(B_r - B)d}{(\bar{\mathbf{v}}_r - \bar{\mathbf{v}})^2 + V_t^2} \tag{2.2}$$

with B as the buoyancy, d as the depth, subscript r represent reference values, $(\bar{\mathbf{v}}_r - \bar{\mathbf{v}})$ denoting the influence of the resolved vertical shear and V_t^2 denoting the influence of unresolved turbulent velocity shear. The boundary layer depth then becomes:

$$h_b = Ri_b \frac{(\bar{\mathbf{v}}_r - \bar{\mathbf{v}})^2 + V_t^2}{(B_r - B)} \tag{2.3}$$

with $Ri_b = 0.3$ (Wallcraft et al., 2009).

2.2   Air-sea interactions

The circulation in the ocean can be divided into two types. The wind-driven currents that primarily are generated by the winds and the thermohaline circulation, which is driven by surface heat and freshwater fluxes (Knauss, 2005). This main focus of this thesis is on the upper-ocean circulation, since the thermohaline circulation is a deep ocean circulation it has no impact on the upper-ocean circulation and will not be discussed further.

2.2.1   Wind-driven currents

The characterization of the atmospheric wind field is that the mid-latitudes have westerlies and at low latitudes near the equator there are easterly trades. This main wind flow creates a circulation in the surface waters of the oceans with a clockwise flow in the Northern Hemisphere and a counterclockwise flow in the Southern Hemisphere. These circulations are called gyres. The two large gyres are separated by a countercurrent, that is located slightly north of the equator in the Atlantic and Pacific oceans (Knauss, 2005).
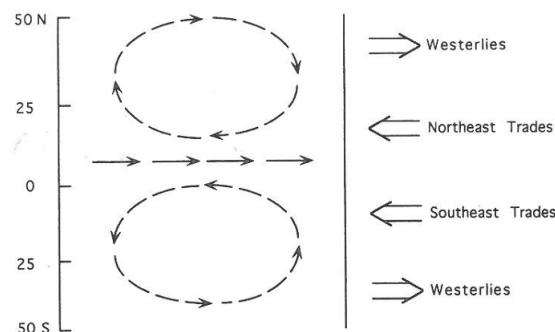
Figure 2.3: The main wind flow creates two current gyres in the world oceans, one clockwise in the Northern Hemisphere and one counterclockwise in the Southern Hemisphere. Source: Knauss (2005).

A simple sketch of how the wind fields affect the oceans and creates current gyres is shown in figure 2.3.

This simple assumption of the wind-driven circulation in the oceans does not hold. If it did, the current gyres should be symmetrical, their strength and direction should be directly affected of the winds and they should be equally strong everywhere. This is not the case. The western boundary currents of the great gyres, such as the Gulf Stream, the Brazil current, the Kuroshio and the East Australian current, are strong and have narrow flows whereas their counterparts on the eastern sides are much weaker and more diffuse (Knauss, 2005).

2.2.2 Mixing in the upper ocean

Mixing is identified as present in two distinct regimes in the oceans: The mixed layer that is influenced by surface forcings, such as heat flux and wind stress, and the ocean interior, where mixing occurs due to internal waves, shear instability and double diffusion (Large et al., 1994).

Mixing occurs in both the horizontal and vertical direction. Horizontal mixing is mixing occurring along surfaces of constant density, isopycnal surfaces, and does not require as much energy as vertical mixing. There is much more mixing along the isopycnals (horizontal mixing) than across the isopycnals (vertical mixing). This is because the vertical mixing works against buoyancy forces, and is hence much smaller than the horizontal mixing (Knauss, 2005). Vertical mixing is the mixing that occurs during a storm passage with enhanced turbulence and mixing of heat down through the water column. The strength of the vertical mixing created at the base of the mixed layer depends on the stratification of the ocean. The higher the stratification, the lower the vertical mixing is according to the increase in energy needed to create the mixing (Knauss, 2005).

The producing of turbulence and mixing can be created by three mechanisms; wind-driven shear of near-surface waters driven by wind stress, transferring energy from the wind stress to oceanic turbulence depending of the magnitude of the wind stress: shear at the base of the mixed layer due to near-inertial motions transferring energy from the wind stress to oceanic turbulence depending on the near-inertial frequency component of the wind stress; and by convective motions due to surface heat fluxes (D'Asaro, 1985).

The entrainment of colder waters can penetrate the top of the thermocline, which deepens the mixed layer. A deepening of the mixed layer is often seen after a storm passage, where the largest response is seen during intense and slowly moving hurricanes. The largest sea surface temperature response is seen where there is a thin initial mixed layer and the temperature gradient in the upper thermocline is sharp, such that cold water is close to the sea surface (Price, 1981).

2.3 Inertial waves

Inertial waves are waves that are possible only in rotating fluids. They are created in the oceans because of the Earths rotation. Inertial waves are oscillations of the inertial frequency, f, in the interior of the ocean (Aldridge & Lumb, 1987).

If a fluid particle is set in horizontal motion in absence of other forces (such as pressure-gradients and frictional forces), the Navier-Stokes relation is reduced to:

$$\begin{aligned}
\frac{DU}{Dt} &= fV \\
\frac{DV}{Dt} &= -fU,
\end{aligned}$$

(2.4)

where $f = 2\Omega \sin(\phi)$ is the Coriolis parameter (also called the inertial frequency) with $\Omega = 7.29 \cdot 10^{-5} \mathrm{s}^{-1}$ as the angular speed of the Earths rotation and ϕ as the latitude, U is

the zonal and V the meridional velocity of the fluid. The solution to equation 2.4 describes an inertial oscillation, with the acceleration of the fluid particle always directed toward the center of the inertial motion (Kantha & Clayson, 2000). The solution to these equations is given as:

$$\begin{aligned} u &= U \sin(ft) \\ v &= U \cos(ft), \end{aligned} \tag{2.5}$$

The period of the inertial motion is given as a function of the Coriolis force:

$$T_i = \frac{2\pi}{f} = \frac{2\pi}{2\omega \sin(\phi)} = \frac{2\pi}{2(\frac{2\pi}{24\text{h}}) \sin(\phi)} = \frac{12\text{h}}{\sin(\phi)}. \tag{2.6}$$

which gives an inertial period at the two mooring locations of 7.15 days at 4°N and 2.4 days at 12°N as shown in table 2.1

	Local inertial period, T_i
4°N	7.15 days
12°N	2.4 days

Table 2.1: The inertial period at the two mooring locations.

A particle set in motion will move in a circular path in the anticyclonic direction, with a constant speed $\tilde{v} = \sqrt{u^2 + v^2}$ with the radius $r_i = \frac{\tilde{v}}{f}$, clockwise in the Northern Hemisphere and counterclockwise in the Southern Hemisphere, due to the Coriolis force (Kantha & Clayson, 2000). An illustration of the inertial motion is shown in figure 2.4(a). When a current passes the inertial wave, it will move with the current flow as shown in figure 2.4(b).

When the wind blows across the oceans it will stir up the water, which causes a perturbation from the oceans equilibrium. The restoring force of the inertial waves in the ocean is the Coriolis force.
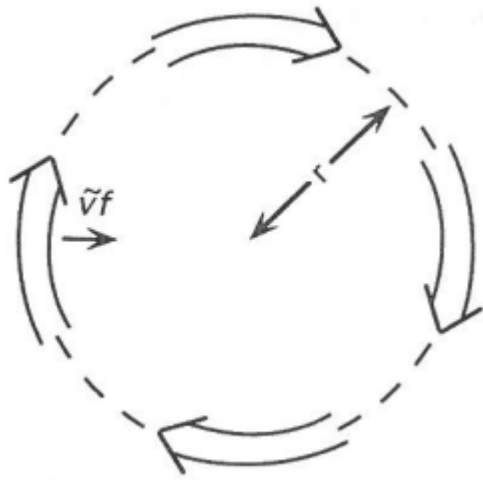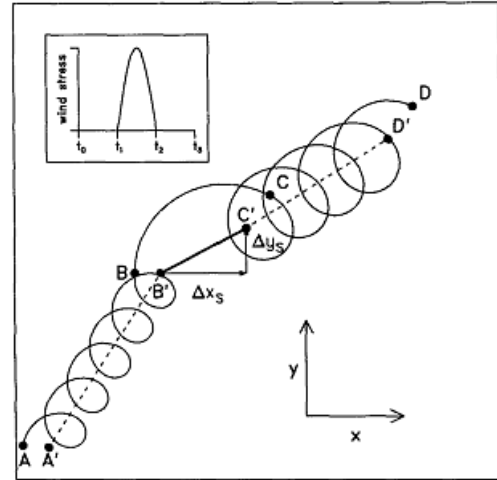
(a) Source: (Knauss, 2005)   (b) Source: (Large & Crawford, 1995)

Figure 2.4: (a) Inertial motion of a particle set in motion with a constant speed of $\tilde{v}$ and the radius r. (b) The motion of an inertial wave that is moving with the current flow.

2.3.1   Coriolis force

If a particle is moving northward in the Northern Hemisphere it will be deflected to the right and if it moves southward in the Southern Hemisphere it will be deflected to the left. This deflection is caused by the fact that the particle is accelerated on a rotating earth (Knauss, 2005).

A particle moving to the north (south) in the Northern Hemisphere is deflected to the right (left) and will hence rotate clockwise (counterclockwise), while a particle moving to the south (north) in the Southern Hemisphere is deflected to the left (right) and will rotate counterclockwise (clockwise). This is shown in figure 2.5. The magnitude of the Coriolis acceleration depends on the latitude, ϕ, and increases with an increasing latitude, such that it will be zero at the Equator and at the two poles it will have the same maximum, but with opposite sign (Knauss, 2005).

The effects of the Coriolis acceleration are expected to be important for features with time scales much longer than the inertial period (such as the Gulf Stream or midlatitude atmospheric weather systems), whereas the Coriolis acceleration can be neglected in short-lived features (such as a tornado or a cumulus cloud). Considering a tornado for instance, it rotates so rapidly on its own axes that it does not really feel the ambient rotation of the earth, hence the Coriolis acceleration can be neglected (Vallis, 2006).
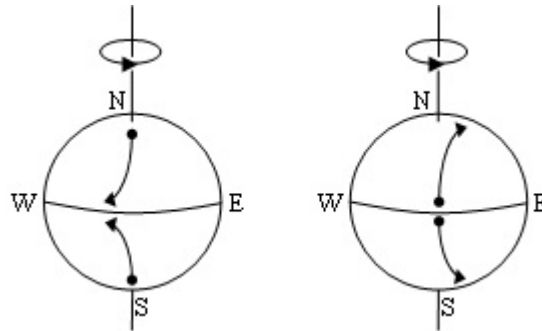
Figure 2.5: The direction of a particle moving in the two hemispheres. A particle moving north in the Northern Hemisphere will be deflected to the right and rotate clockwise, while a particle moving south in the Southern Hemisphere will be deflected to the left and rotate counterclockwise. Source (Hadley, 2010).

2.3.2   Near-inertial waves

Near-inertial waves are inertial waves that have propagated away from their origin. Their frequency will be close to the local inertial frequency, $f \approx f_I$ (Garrett, 2001).

Assuming that the ocean is horizontally homogeneous and that the mixed layer velocity is vertically uniform, the acceleration is balanced by the Coriolis force to zeroth order

$$\frac{dU}{dt} + ifU = 0, \tag{2.7}$$

with $U = u + iv$ representing the horizontal current components. To first order, the wind stress, represented by $T = \frac{\tau_x + i\tau_y}{\rho H}$, and friction are added, such that

$$\frac{dU}{dt} + ifU = T - rU, \tag{2.8}$$

ρ being the density and H the mixed layer depth, τ_x is the wind stress in the zonal direction and τ_y is the wind stress in the meridional direction. Using an appropriate mixed layer depth, this model, including the empirical "decay parameter" r, makes good predictions of the mixed layer inertial currents (D'Asaro et al., 1995).

Near-inertial waves are large contributors to the deepening of the mixed layer. When the mixed layer is deepened, the sea surface temperature will change. Water below the sea surface is colder than the surface temperature, hence a deepening of the mixed layer will contribute to a cooling of the sea surface temperature (at high latitudes, the sea surface temperature of the water is colder than the water below, hence a mixing will cause a heating of the sea surface temperature). This change in temperature affects the uptake of energy in the oceans since colder oceans hold less energy than warmer oceans.

The decay of inertial waves in the mixed layer is thought to propagate through the ocean, down through the thermocline to the deep oceans. This assumption is supported by observations that show increased near-inertial motions in the thermocline during mid-latitude storms and hurricanes (D'Asaro et al., 1995).

The biggest contributor to the generation and dissipation of near-inertial waves is the wind (D'Asaro et al., 1995).

The evolution of the near-inertial waves can be described by the linear equation of motion.

$$\frac{\partial \tilde{U}_{In}}{\partial t} = i\frac{c_n^2}{2f_0}\nabla_H^2 \tilde{U}_{In} + i(f(y) - f_0)\tilde{U}_{In} \tag{2.9}$$

where $\nabla_H^2 \tilde{U}_{In}$ expresses the horizontal scale of the mixed layer inertial currents. It is assumed that the current, U_{In}, varies slowly compared to the Coriolis parameter, f^{-1}. The Coriolis frequency, $f(y)$, varies as a function of the north-south distance. From this the dispersion relationship for near-inertial motions can be produced:

$$\omega_n - f = \frac{c_n^2}{2f}\alpha^2, \tag{2.10}$$

with ω_n being the frequency, c_n^2 the modal phase speed and $\alpha^2 = k^2 + l^2$, is the horizontal wavenumber component with k and l as the component in the east and north direction (D'Asaro et al., 1995).

If the mixed layer base is displaced by a divergence of the mixed layer oscillating inertial currents, a pressure gradient will be produced in the thermocline, which accelerates the inertial currents at depth. The horizontal scale of the mixed layer inertial currents determines the rate of energy transfer, small-scale mixed layer inertial currents propagate more rapidly than large-scale mixed layer inertial currents.

2.4   Isolating oceanic near-inertial motions

In order to isolate the oceanic near-inertial motions the near-inertial velocity is determined. The near-inertial velocity is the velocity of the near-inertial waves in the oceans.

There are two methods to determine the near-inertial velocity. One method is determining the variance of the near-inertial spectral band. This is done as an integral of the spectrum of the current time series in the limits of the band. From the near-inertial variance it is possible to find the near-inertial velocities. The second method uses a Butterworth bandpass filter in the near-inertial frequency band to filter the current time series. The near-inertial velocity is here defined as the mean of the near-inertial current speed averaged over the inertial period, T_i.

2.4.1   Near-inertial variance

Parseval's theorem states that

$$\int_{-\infty}^{\infty} |x(t)|^2 dt = \int_{-\infty}^{\infty} |X(f)|^2 df \tag{2.11}$$

with $x(t)$ being the filtered time series and $X(f)$ being the frequency spectrum of the time series in the near-inertial band to a good approximation, since $X(f) = S(f' \in [0.7f; 1.3f])$ (Riley et al., 2006). The variance, σ^2, of the near-inertial band is therefore determined by

$$\sigma^2 = \int_{0.7f_I}^{1.3f_I} |S(f)|^2 df,$$ \hfill (2.12)

where $|S(f)|^2$ is the frequency spectrum and $f_I = 2\Omega \sin(\phi)$ is the local inertial frequency, with $\Omega \approx 10^{-5} s^{-1}$ as the rotational frequency of the earth and ϕ is the latitude.

In order to have a variance in both directions, the variance in the zonal and meridional directions are added

$$\sigma^2 = \sigma_u^2 + \sigma_v^2,$$ \hfill (2.13)

which is only possible assuming that the variances are independent.

2.4.2 Butterworth bandpass filter

A Butterworth bandpass filter is a signal processing filter that lets frequencies of a certain range pass through and rejects all frequencies outside this range (Kanasewich, 1981).

Since the Butterworth bandpass filter is used to find the near-inertial velocity, the range in which the filter is used will be the near-inertial frequency band ranging between $0.7f_I - 1.3f_I$.

The near-inertial velocity is the square-root of the squared filtered velocities:

$$|U_{NI}| = \sqrt{(u^2 + v^2)}.$$ \hfill (2.14)

3 Data

All data used during this thesis comes from moorings and from the forced simulation of the Community Earth System Model (CESM). This chapter holds a description of the moorings including a description of the parameters from the moorings that are used in this thesis, and a description of the CESM including a description of the air-sea fluxes used and a model quality discussion.

3.1 Moorings

All information in this section are based on information from (Servain et al., 1998) and (Bourles et al., 2008) unless otherwise specified.

Moorings are floated buoys that are anchored at the sea. The moorings used in this thesis are Autonomous Temperature Line Acquisition System (ATLAS) moorings from the Pilot Research Moored Array in the Tropical Atlantic (PIRATA) project. A picture of a mooring placed at sea is shown in figure 3.1.

Figure 3.1: A picture of an ATLAS mooring positioned at sea. Modified from: NOAA (webA).

The ATLAS moored buoys measure oceanic properties of temperature, salinity and conductivity between the surface and 500 meters depth. The moorings also measure surface

meteorological variables such as wind speed, wind direction, air temperature, humidity, rainfall and solar radiation. The design of the ATLAS mooring is seen in figure 3.2(a). The wind is measured by the wind sensor, which is placed on top of the mooring in 4 meters height. The short wave, air temperature and relative humidity sensor as well as the rain gauge and the data logger/transmitter are all placed above the ocean on the toroidal buoy, which is 2.3 meters in diameter. Under the sea surface there is a conduction cable and an mooring line at which all subsurface sensors for measuring temperature, conductivity and pressure are placed. The sea surface temperature and conductivity sensors are placed at 1 meter depth. The mooring is anchored to the bottom of the ocean by an anchor at the end of the mooring line. The sensors at the mooring line transmit the measurements below the surface to the surface buoy. Current velocities are measured using a subsurface Acoustic Doppler Current Profiler (ADCP) mooring. The design of an ADCP mooring is seen in figure 3.2(b). Usually ADCPs are installed in tandem with a nearby ATLAS mooring. Near the surface, where acoustic backscatter from the sea surface interferes with the ADCP signal, the ATLAS mooring can provide current velocities, as well as they can measure current velocity as a backup to the ADCP (NOAA, webB).
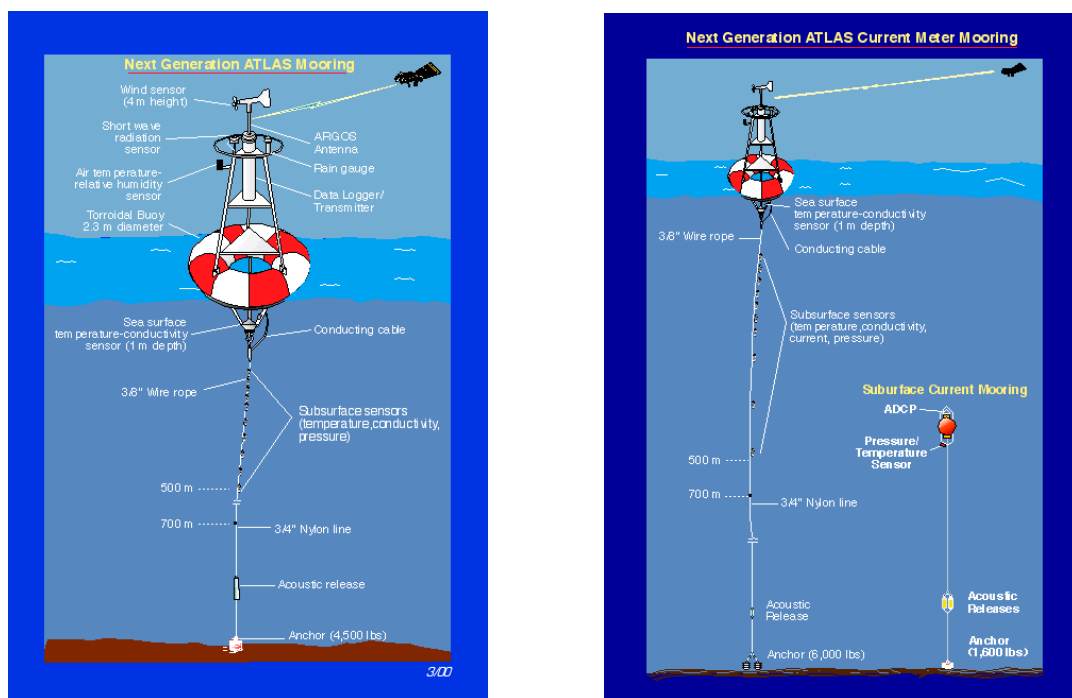
(a) Source: NOAA (webB)   (b) Source: NOAA (webB)

Figure 3.2: The design of an (a) ATLAS and an (b) ADCP mooring.

The PIRATA project was developed in the late 1997 involving Brazil, France and the United States as a multinational observation network. There were a lot of unresolved issues concerning the ocean-atmosphere interactions in the tropical Atlantic. Therefore a further investigation of the tropical Atlantic needed to be done.

Figure 3.3 shows the backbone and extensions of the ATLAS buoys in the PIRATA project. The backbone (red squares) buoys were set out in the period from September 1997 - March 1999. The PIRATA Southwest Extension (green circles) was initiated in August 2005, the PIRATA Southeast Extension (yellow triangle) was implemented as a pilot phase in June 2006, and the PIRATA Northeast Extension (blue stars) was implemented in June 2006 and May 2007.
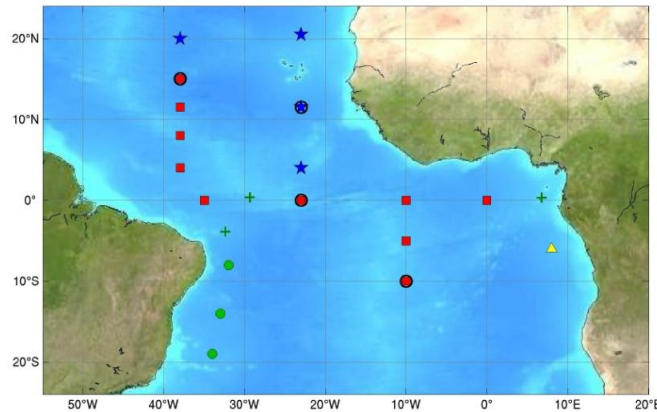
Figure 3.3: The backbone array (red squares) of the PIRATA project, including the extensions made through the years, where the green circles represent the Southwest Extension, the yellow triangle representing the Southeast Extension and the blue stars representing the Northeast Extension. The green crosses indicate three island-based observational sites. The four buoys with a black circle (three from the backbone array and one from the Northeast Extension) are buoys with barometers and the ability of estimating net heat fluxes. Figure from (Bourles et al., 2008).

The PIRATA program was developed in order to improve the description of the seasonal-to-interannual variability in the upper ocean and the air-sea interface in the tropical Atlantic, and to improve the understanding of the surface heat flux and ocean dynamics contributions to the seasonal and interannual variability of SST within the tropical Atlantic basin.

Before the PIRATA project started, data were collected by volunteer observing ships (VOS), the $1982-1984$ Français−Océan−Climat Atlantique Equatorial/The Seasonal Response of the Equatorial Atlantic (FOCAL/SEQUAL) experiment, tide gauge stations, drifting buoys and satellite experiments. All of these methods have some problems and none of them give very good data from the equatorial Atlantic region, which means that there was a limited knowledge of the equatorial Atlantic region.

The parameters that are used in this thesis are the current velocities, measured at the mooring stations at 10 meters depth in units of cm/s, the sea surface temperature in units of °C, temperatures in the 12 different depths available (10 meters, 13 meters, 20 meters, 60 meters, 80 meters, 100 meters, 120 meters, 140 meters, 180 meters, 300 meters and 500 meters) also measured in °C and the wind velocities, measured 4 meters above the sea surface in units of m/s. The wind velocities are converted to wind stress by the equations:

$$\tau_x = \rho_{air} \cdot c_d \cdot |U|^2 = \rho_{air} \cdot c_d \cdot \frac{(u^2 + v^2)}{\sqrt{u^2 + v^2}} \cdot u^2 \tag{3.1}$$

$$\tau_y = \rho_{air} \cdot c_d \cdot |V|^2 = \rho_{air} \cdot c_d \cdot \frac{(u^2 + v^2)}{\sqrt{u^2 + v^2}} \cdot v^2 \tag{3.2}$$

with the lowercase x denoting the zonal and y the meridional direction, $c_d = 1.3 \cdot 10^{-3}$ is the dimensionless aerodynamic drag coefficient and $\rho_{air} = 1.225$ kg/m^3 is the air density, u is the wind in the zonal direction and v is the wind in the meridional direction.

The temporal resolution of the PIRATA mooring varies depending on the parameters wanted and the location of the mooring. The temporal resolutions available are high resolution (varying from 2 seconds to 1 hour), daily, 5-day, monthly and quarterly. This thesis uses the highest resolution possible for each parameter, which is 10 minutes for the winds and temperature, 20 minutes for the currents at 4°N and 10 minutes for the currents at 12°N.

Failed measurements in the current velocities (reported as $u_{cur} = v_{cur} = -999.9$ cm/s), temperature (reported as $T = -9.9$°C) and wind (reported as $u_{wind} = v_{wind} = -99.9$ m/s) are removed with a simple interpolation, by replacing it with the mean of the two surrounding values. If there are two or more consecutive readings that contain failed measurements, data is replaced with the value of the previous good measurement. NaN's can occur between timesteps, which indicates that they are artificially produced data by an equipment error. These are replaced in the same way as the failed measurements.
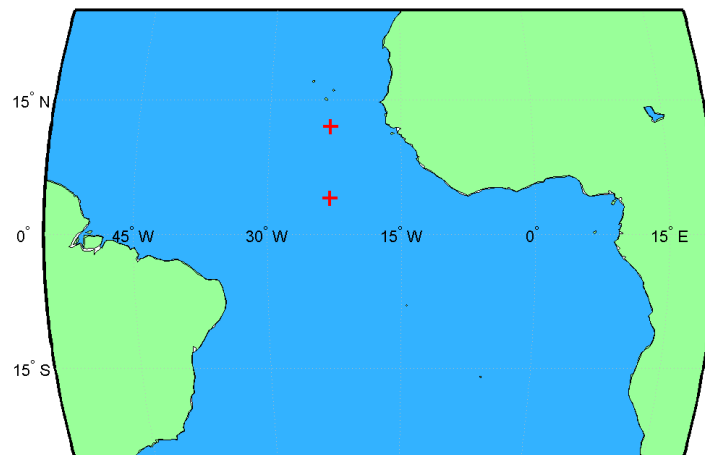
Figure 3.4: The location of the two mooring positions, 4°N 23°W and 12°N 23°W, indicated with red crosses.

The tropical moorings, used in this thesis, are selected to be moorings that are off Equator and at two different latitudes. Some important criteria in the choosing of mooring sites are that they should be off Equator, they should contain wind and current data in both the zonal and meridional direction and that they should contain temperatures in different

depths. These criteria are important because these data are crucial for determining inertial waves and changes in the mixed layer as well as their origin. The moorings chosen are from the PIRATA Northeast Extension, and are located at 4°N 23°W and 12°N 23°W, shown with red markings in figure 3.4.

3.2   The Community Earth System Model

The Community Earth System Model (CESM) is developed from the original Community Climate Model (CCM), that was created by the National Center for Atmospheric Research (NCAR) in 1983 (UCAR, webA). The CESM consist of the fully coupled atmosphere, ocean, land and sea-ice models.

This study uses a simulation of the CESM, that is forced with observed atmospheric air-sea flux fields by Large & Yeager (2004). The ocean is forced by the freshwater, F, heat, Q, and momentum, $\vec{\tau}$, fluxes.

The ocean surface fluxes are given by:

$$F = f_0 F_{as} + (1 - f_0)F_{io} + R \tag{3.3}$$
$$Q = f_0 Q_{as} + (1 - f_0)Q_{io} \tag{3.4}$$
$$\vec{\tau} = f_0 \vec{\tau}_{as} + (1 - f_0)\vec{\tau}_{io} \tag{3.5}$$

with as denoting the air-sea fluxes and io denoting the ice-ocean fluxes, f_0 is a fraction of an Ocean General Circulation Model (OCGM) grid point and R is the continental runoff (explained thoroughly in Large & Yeager (2004)). This study only works on low latitudes, where there is no sea-ice, $f_0 = 1$, which will make the ice-ocean flux terms zero: $(1 - f_0)F_{io} = (1 - f_0)Q_{io} = (1 - f_0)\vec{\tau}_{io} = 0$. The fluxes will then be given by

$$F = F_{as} + R \tag{3.6}$$
$$Q = Q_{as} \tag{3.7}$$
$$\vec{\tau} = \vec{\tau}_{as} \tag{3.8}$$

The computation of the air-sea heat and freshwater fluxes is done by summing estimates of their components:

$$Q_{as} = Q_S + Q_L + Q_E + Q_H + Q_P \tag{3.9}$$
$$F_{as} = P + E \tag{3.10}$$

with Q_S as the solar radiation, Q_L the longwave radiation, Q_E is the latent heat flux, Q_H the sensible heat flux and Q_P is the precipitation heat flux. P is the precipitation and E the evaporation. All fluxes are defined to being positive downwards, such that they are positive when heat, water or momentum goes into the ocean (Large & Yeager, 2004).

The Coordinate Ocean Research Experiments (CORE) is a coupled ocean-ice model, where the air-sea fluxes are computed from prognostic sea surface temperatures. Large & Yeager (2009) used the CORE.v2 that is extended from the CORE.v1 (1958-2000) so that it goes through 2006. A more recent version of the fluxes is extended through 2009 and is the version used during the work with the this thesis. Large & Yeager (2009) used the forced simulation in order to reduce known biases and to evaluate the approach in producing global air-sea fluxes over recent decades and how successful it was.

In the CORE.v2 reanalysis previously known biases are adjusted by comparing with observations. There are still biases in the CORE.v2, but they are not as large as they would have been if the reanalysis had not been adjusted. The climatology air sea heat flux imbalance would, without adjustments, have been 30 W/m^2, whereas with the adjustments made the imbalance over the 23 years $(1984 - 2006)$ becomes about 2 W/m^2. The climatology freshwater fluxes would without any adjustments be 3.5 mg/m^2, with the adjustments, the imbalance in freshwater fluxes is only about -0.1 mg/m^2. The wind stress is compared to two different shipboard wind observations. In the zonal direction the largest biases in the wind stress are in the Pacific Ocean around equator, and in the North Atlantic Ocean. Elsewhere the wind stresses have approximately the same strength. In the meridional direction the strength of the wind stresses are not as equal as in the zonal direction. The wind stress is more biased overall. The largest biases are, however, found in the North and South Atlantic and Pacific. The only place where they really are of comparable strength are around equator (Large & Yeager, 2009).

The ocean component of the CESM level coordinate model is based on the Parallel Ocean Program version 2 (POP2). The ocean model uses a nominal grid resolution of 1°, with 320×384 zonal and meridional grid points respectively. In the zonal direction, the model has a uniform resolution of 1.125°, whereas it has a varying resolution in the meridional direction, varying from 0.27° at the equator to approximately 0.7° in high latitudes (Danabasoglu et al., 2006). Vertically the model has 60 levels, with the highest resolution in the upper ocean, where the resolution is uniformly distributed of 10 meters in the upper 160 meters. The grid North Pole is displaced into Greenland at 80°N 40°W. The minimum ocean depth is set to 30 meters whereas the maximum ocean depth is set to 5500 meters (Danabasoglu et al., 2012). The model output used in this thesis are the wind stress, ocean currents, sea surface temperature and the boundary layer depth. Unfortunately the temperatures are not available in other depths than at the sea surface. It would be very interesting looking at the temperature throughout the mixed layer to look into details of how simulated mixing by near-inertial waves compares with the moorings for strong storm events. Instead the boundary layer depth is used, this can be used to approximate the mixed layer deepening during the storm.

Danabasoglu et al. (2012) investigates the Community Climate System Model version 4 (CCSM4) ocean component and how well it performs in relation to the earlier version CCSM3 and observations. The CCSM4 is the previous version of the CESM model. Figure 3.5(a) shows the sea surface temperature difference distribution of the CCSM4 model versus observations. The global mean bias of the sea surface temperature in CCSM4 is of $+0.33°$C and the corresponding root-mean square (rms) value is 1.15°C, both of which are

improvements in relation to the CCSM3 ($-0.59°$C and rms $1.34°$C). The major biases of the sea surface temperature are the Gulf Stream and its extension into the subpolar North Atlantic and the warm sea surface temperature bias, originating in upwelling regions in the eastern regions of the Atlantic and Pacific oceans, along the western coasts of North and South America and South Africa. Regions where the model generally performs well are along equator and in the western regions of the Pacific Ocean, as well as in a region of the western South Atlantic and in the north-eastern Indian Ocean (Danabasoglu et al., 2012).
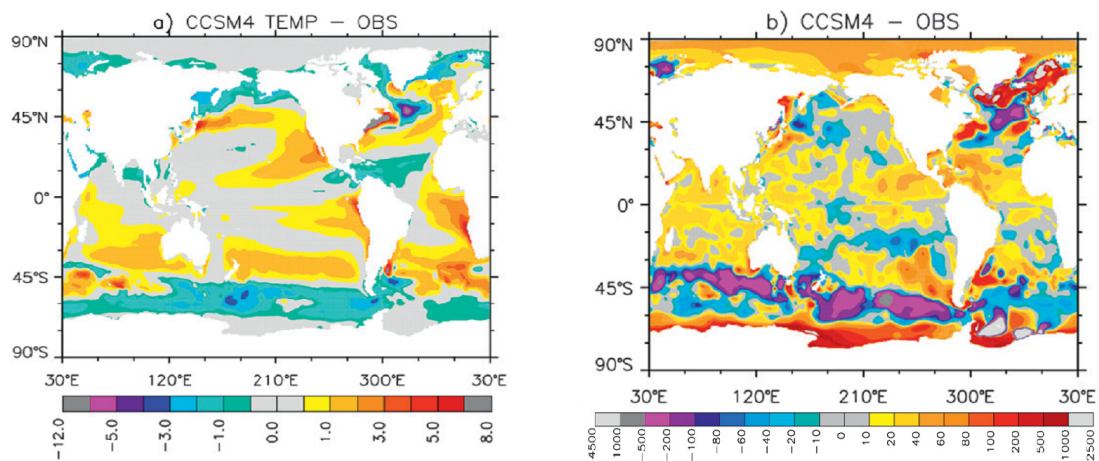
(a) Modified from Danabasoglu et al. (2012), such that the colorbar is shown.

(b) Modified from Danabasoglu et al. (2012) such that the latitude axis and the colorbar are shown.

Figure 3.5: Model quality control of (a) sea surface temperature and (b) mixed layer depth, CCSM4 minus observations.

The quality of the mixed layer depth is shown in figure 3.5(b). The rms value for the mixed layer depth is 173 m, which is a significant difference from the observations. Comparing with the rms value of the CCSM3 (252 m) it is clear that there has been made huge improvements to the mixed layer depths. The largest bias occur in the Southern ocean, northern North Atlantic and in the Greenland-Iceland-Norway (GIN) Seas, which all are areas or relatively poor observational data. The model performs best in the North Pacific and around equator (Danabasoglu et al., 2012).

4 Results

This thesis works with three case studies. First case study is the investigation of near-inertial waves generated at 12°N 23°W during the passage of Hurricane Helene. Second and third case studies will be an investigation of the interaction between near-inertial waves and wind at two different locations, 4°N 23°W and 12°N 23°W.

4.1 Near-inertial waves and hurricanes

The mooring data used for this case study are from 12°N 23°W in the period 1 September 2006 to 1 November 2006, which is around the time Hurricane Helene passed the mooring site. This will make it possible to see how well the model performs in a hurricane situation. Secondly it should be possible to see how the near-inertial waves are affected by a hurricane. Hurricane Helene was strongest at 12°N 23°W on the 12 September 2006.
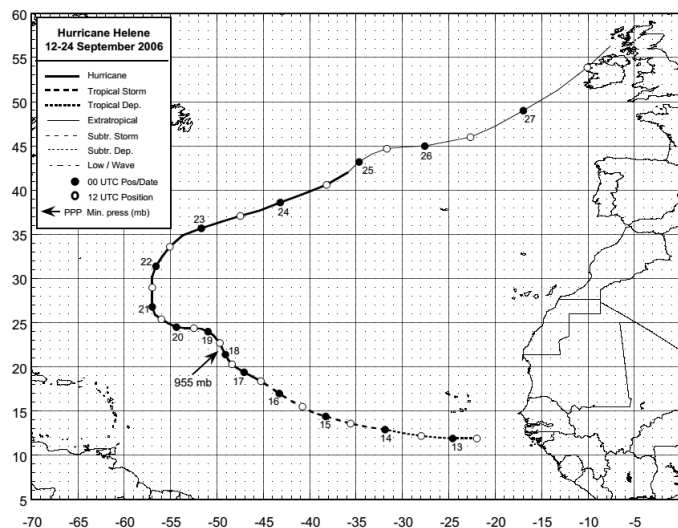
Figure 4.1: Best track of Hurricane Helene, $12 - 24$ September 2006. It is seen that, passing the 12°N 23°W mooring site, Hurricane Helene was a tropical depression. Source: Brown (2007)

The track of Hurricane Helene is shown in figure 4.1. It can be seen that passing the 12°N 23°W mooring site, Hurricane Helene is indicated as a tropical depression. This is

also shown in table 4.1, which is a sample of the values in table 1 from Brown (2007), showing the best track of Hurricane Helene including the pressure, wind stress and the stage of the hurricane during the passage of the mooring site.

| Date/Time (UTC)	Latitude (°N)	Longitude (°W)	Pressure (mb)	Wind speed (kt)	Stage
12/1200	11.9	22.0	1007	25	Tropical depression
12/1800	11.9	23.2	1007	30	Tropical depression
13/0000	11.9	24.6	1007	30	Tropical depression
13/0600	12.0	26.1	1007	30	Tropical depression

Table 4.1: Sample of the values in table 1 from Brown (2007), showing the best track of Hurricane Helene.

Figure 4.2 shows the zonal (4.2(a)) and meridional (4.2(b)) wind stresses for the model (blue lines) and the observations (red lines). The black dashed line is the observed maximum in the zonal wind stress and will be found in the current and temperature figures as well in order to see which effect the wind stress has on the other components. The overall structure of the model is the same as the observations, but the peaks are not as high.

It is clear when the hurricane reaches the mooring at 12°N 23°W. The zonal wind stress peaks first the 12th September with a peak of 0.27 N/m^2, and shortly after the meridional wind stress peaks as well, with a peak of 0.25 N/m^2. The peaks are both in the observations and in the model, but in the model they are much smaller (0.08 N/m^2 in the zonal direction and 0.10 N/m^2 in the meridional direction) than the observations, and standing alone they would not be analyzed as a hurricane.

(a)   (b)
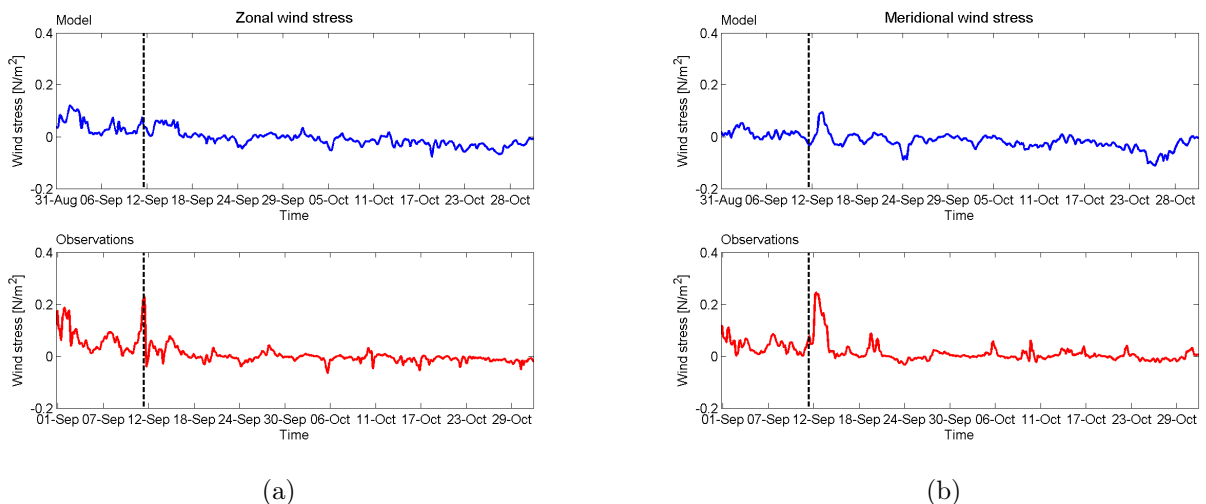
Figure 4.2: The wind stress of the model (blue curve) and the observations (red curve) in the (a) zonal and (b) direction. The black dashed line indicates where the observed zonal wind stress has its maximum.
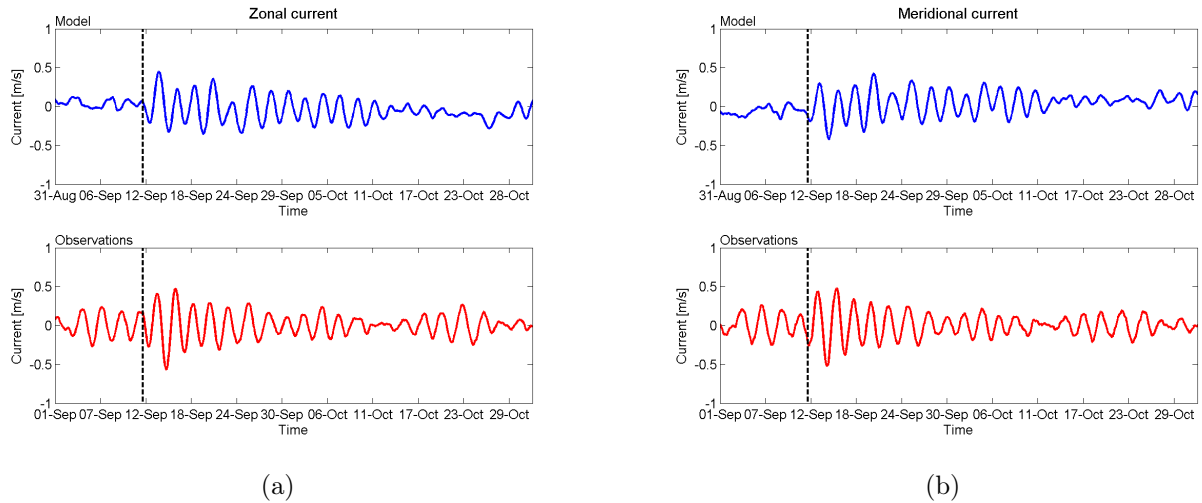
Figure 4.3: The (a) zonal and (b) meridional currents of the model (blue curve) and observations (red curve). The black dashed line indicate where the observed zonal wind stress has its maximum.

Figure 4.3 shows zonal (4.3(a)) and meridional (4.3(b)) currents for the model (blue lines) and observations (red lines). The black dashed line indicates where the observed zonal wind stress has its maximum. It is clear that the model and observations follow the same pattern here. Some of the waves in the observations are not seen in the model in particular before the zonal wind stress maximum in the beginning of the storm.

The observed currents have a larger amplitude than the currents of the model. In the zonal direction, the maximum amplitude just after the winds stress maxima is 0.98 m/s for the observations whereas the model amplitude at the same time is 0.77 m/s. In the meridional direction the amplitude of the observations is 0.95 m/s and the amplitude of the model is 0.72 m/s.

The sea surface temperature of the model (blue line) and observations (red line) is shown in figure 4.4. The black dashed line again indicates where the observed zonal wind stress has its maximum. Around the 22 October the observations show a trough in the sea surface temperature.

There is an error in the model output, such that there is no diurnal cycle in the model temperatures. The diurnal cycle in the observations is averaged out, such that the model can be compared to the observations. The error has been corrected for future users of the forced simulation CESM output.

The model currents are generally in agreement with the observations, though the fluctuations on the model output are smaller than the observed fluctuations. The temperature decrease in the hurricane is of 1.6°C in the observations, which is double of that of the model. The model temperature decrease is 0.8°C.
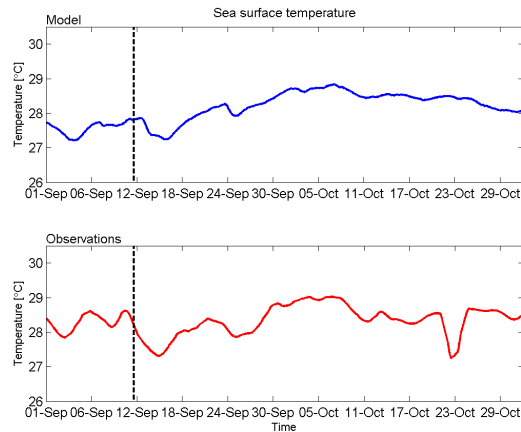
Figure 4.4: Sea surface temperature for the model (upper) and the observations (lower). The black dashed line indicates where the observed zonal wind stress has its maximum. There is seen a clear decrease in the sea surface temperature during the hurricane. Around the 22 October there is a trough in the sea surface temperature.

The moorings measure the temperatures in 12 different depths. Figure 4.5 shows the temperatures with depth. The black dashed line again indicates where the observed zonal wind stress has its maximum. It can be seen that the temperature in the top layers (0-20 meters) starts to decrease when the wind stress is increased, but before the maximum wind stress. It is not quite clear what happens to the temperatures from 60 meters and down, therefore figures, zooming in on the depths, are made. They are shown in the following figures and commented in the following paragraphs.
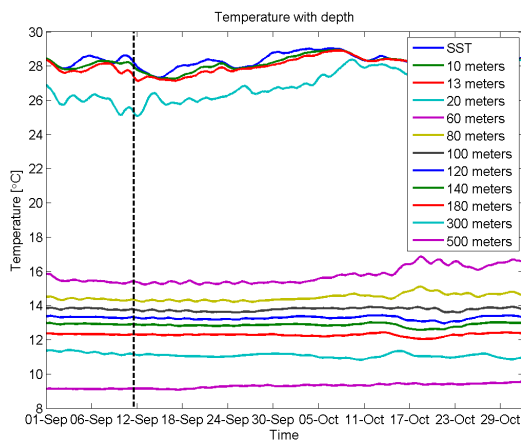
Figure 4.5: The temperatures in 12 different depths, going from the sea surface to 500 meters depth. The black dotted line indicates the time where the observed zonal wind stress has its maximum.

Figure 4.6(a) shows the temperatures in the top layers. The blue line is the sea surface temperature, the green line is the temperature in 10 meters depth, the red line is the temperature in 13 meters depth and the cyan line is the temperature in 20 meters depth. It can clearly be seen that the temperature starts to change as the wind stress increases, and not at the maximum wind stress. The sea surface temperature decreases by 1.3°C, the temperature in 10 meters depth decreases by 1.0°C, the temperature in 13 meters depth decreases by 0.6° and the temperature in 20 meters depth increases by 1.3°C. This temperature decrease in upper layers and increase in 20 meters is an indication of vertical mixing. It is not only during the passage of the storm indications of mixing are seen. Around the 26 September and 8 October there is also a decrease in temperature at surface, 10 and 13 meters depth and an increase in the 20 meter temperature.
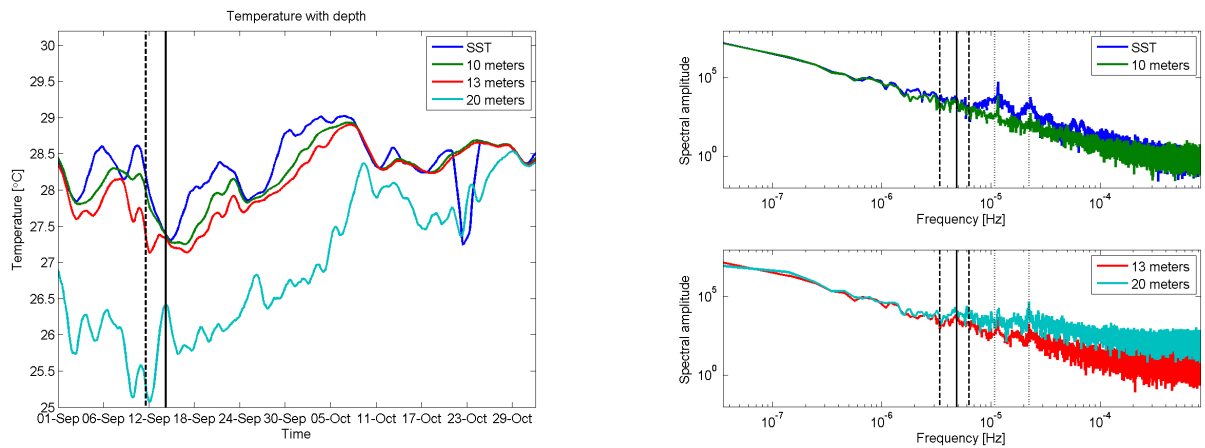
(a) Sea surface temperature (blue) and temperature in 10 meters (green), 13 meters (red) and 20 meters (cyan) depth. The black dashed line indicates where the observed zonal wind stress has its maximum and the black solid line indicates the time where the sea surface temperature and the 20 meters temperature are closest, indicating vertical mixing.

(b) Frequency spectrum of the temperatures at sea surface (blue), 10 meters (green), 13 meters (red) and 20 meters (cyan) depth. The black dashed lines indicate the near-inertial frequency band and the black solid line indicates the inertial frequency. The black dotted lines show the frequencies for the diurnal cycle and the M2 tide.

Figure 4.6

Looking at frequency spectra it is expected that there will be a notable peak at the diurnal cycle, located at $\frac{1}{24\text{h}} = \frac{1}{86400\text{s}} = 1.16 \cdot 10^{-5}$ Hz, and at the M2 tide, located at $\frac{1}{12\text{h}} = \frac{1}{43200\text{s}} = 2.31 \cdot 10^{-5}$ Hz. For some parameters and at some depths it is also expected that there will be a notable peak in the near-inertial frequency band. The range of the near-inertial frequency band at 12°N 23°W is shown in table 4.2.

Figure 4.6(b) shows the spectrum of the temperatures in depths 0-20 meters. At the sea surface the diurnal cycle and the M2 tide are clearly seen, but there is no notable peak in the near-inertial frequency band, which is shown with black dashed lines, the black solid line is the inertial frequency. The frequency spectra at 10-20 meters all have a notable peak at the diurnal cycle and at M2 tide, but no notable peak in the near-inertial frequency

$0.7f_i$	f_i	$1.3f_i$
$3.38 \cdot 10^{-6}$ Hz	$4.83 \cdot 10^{-6}$ Hz	$6.27 \cdot 10^{-6}$ Hz

Table 4.2: The near-inertial frequency band is located between $0.7f_i$ and $1.3f_i$, where $f_i = 2\omega \sin(\phi)$. At 12°N 23°W the near-inertial band is located at these values.

band. The oscillations occurring in these depths do not look inertial, so it was not expected that there should be a notable peak in the near-inertial frequency band. This is confirmed by the spectrum showing no notable peak in the near-inertial frequency band.

Figure 4.7(a) shows the temperature in 60 meters (pink line) and 80 meters depth (yellow line). The temperature seems to be directly affected by the changes in wind stress and current as it starts to oscillate during the storm. This could be an indication of vertical mixing. The temperature oscillations are in the order of 0.2°C at 60 meters and 0.1°C at 80 meters. There is a much larger temperature variability around 20 October. The oscillations could be inertial oscillations, this is examined by making a frequency spectrum of the temperatures of these depths, shown in figure 4.7(b). There is a notable peak in the near-inertial frequency band, which means, as expected, that the oscillations in figure 4.7(a) are inertial oscillations. The diurnal cycle is not visible at these depths, but the M2 tide is clear in the frequency spectrum.
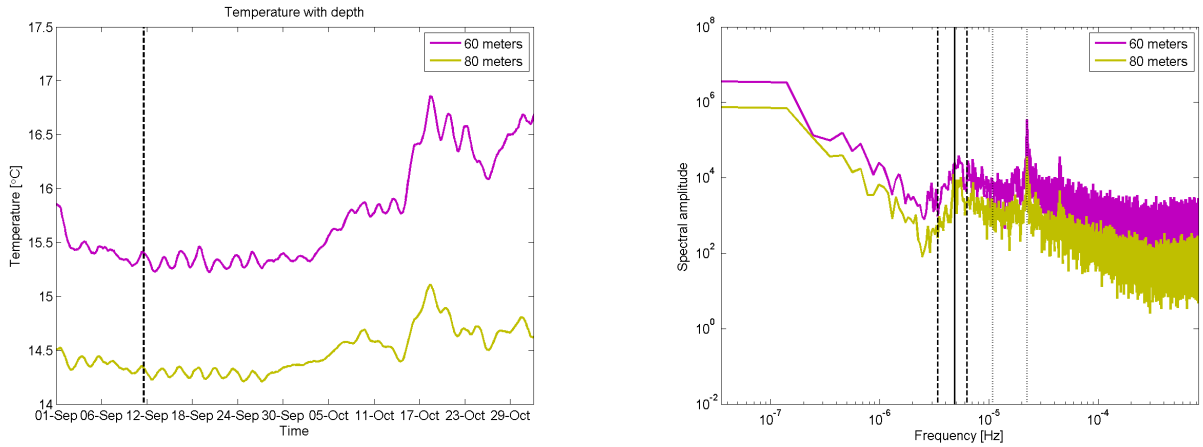
(a) Temperature in 60 meters and 80 meters depth. The black dashed line indicates where the observed zonal wind stress has its maximum.

(b) Frequency spectrum of the temperatures at 60 meters and 80 meters depth. The black dotted lines show the frequencies for the diurnal cycle and the M2 tide. The black dashed lines indicate the near-inertial frequency band and the black solid line indicates the inertial frequency.

Figure 4.7

Figure 4.8 shows the temperatures in 100 (black), 120 (blue) and 140 meters depth (green). The temperature oscillates with a amplitude of 0.13°C in 100 meters, 0.1°C in 120 meters and of 0.05°C in 140 meters during the storm. The temperatures at these depths show the same behavior as the temperatures at 60 and 80 meters. The frequency spectrum of the temperatures is shown in figure 4.8(b). As expected, it is clear that the oscillations are inertial. At these depths there is also a notable peak at the M2 tide. The peak of the diurnal cycle is very weak.

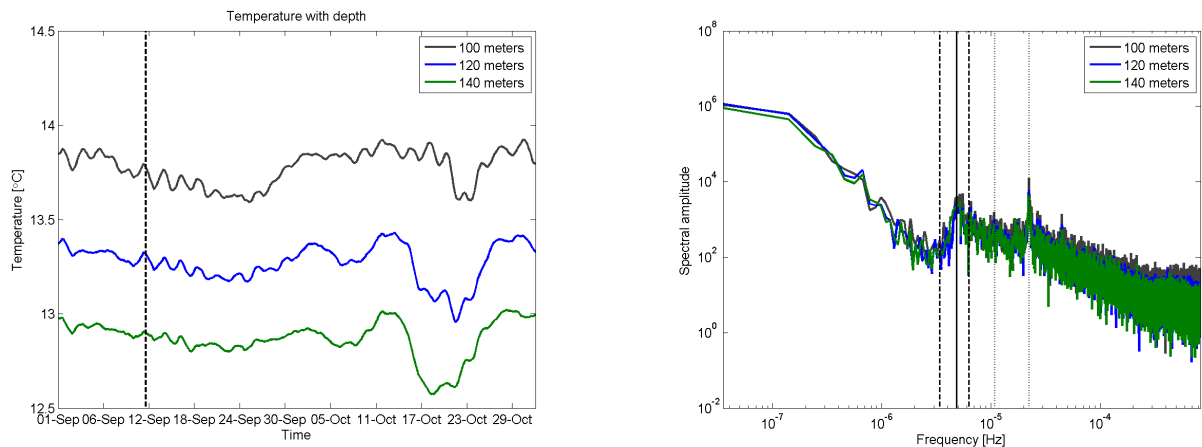(a) Temperature in 100 meters, 120 meters and 140 meters depth. The black dashed line indicates where the observed zonal wind stress has its maximum.

(b) Frequency spectrum of the temperatures at 100 meters, 120 meters and 140 meters depth. The black dotted lines show the frequencies for the diurnal cycle and the M2 tide. The black dashed lines indicate the near-inertial frequency band and the black solid line indicates the inertial frequency.

Figure 4.8

Below 140 meters, at 180 (red), 300 (cyan) and 500 meters depth (pink), seen in figure 4.9, there is not much response to the increase in wind stress. This is what was expected since these depths are at the base of and below the mixed layer, and the wind-driven mixing only extends through the mixed layer and a little bit below. The temperature in 180 meters decrease with 0.02°C, at 300 meters with 0.08°C and at 500 meters with 0.01°C. Looking at the frequency spectrum (figure 4.8(b)), it is seen that, there is a notable peak in the near-inertial frequency band, indicating inertial oscillations, but the peak at the M2 tide is much more notable and the one at the diurnal cycle is also higher, indicating that the inertial waves at these depths are very weak, which is consistent with what is seen in figure 4.9(a), and with the expectations.
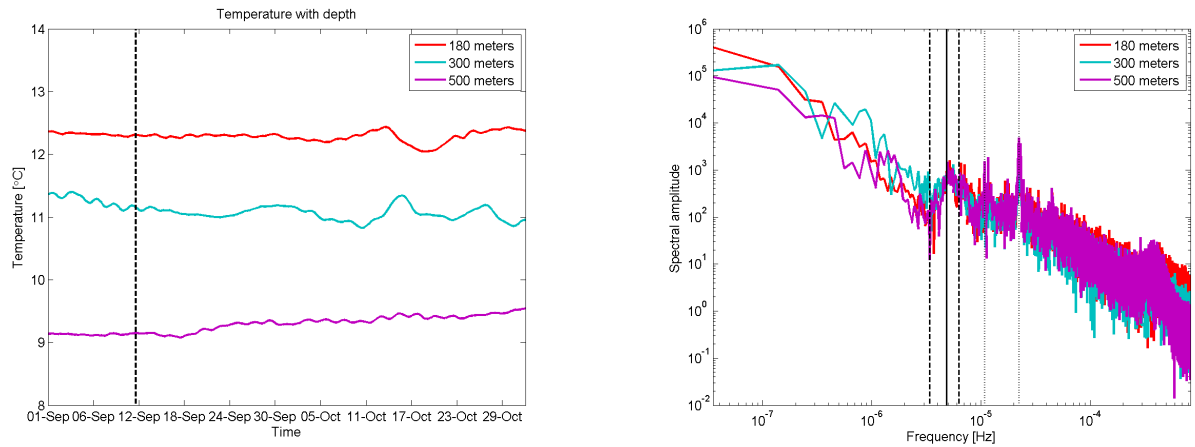
(a) Temperature in 180 meters, 300 meters and 500 meters depth. The black dashed line indicates where the observed zonal wind stress has its maximum.

(b) Frequency spectrum of temperature at 180 meters, 300 meters and 500 meters depth. The black dotted lines show the frequencies for the diurnal cycle and the M2 tide. The black dashed lines indicate the near-inertial frequency band and the black solid line indicates the inertial frequency.
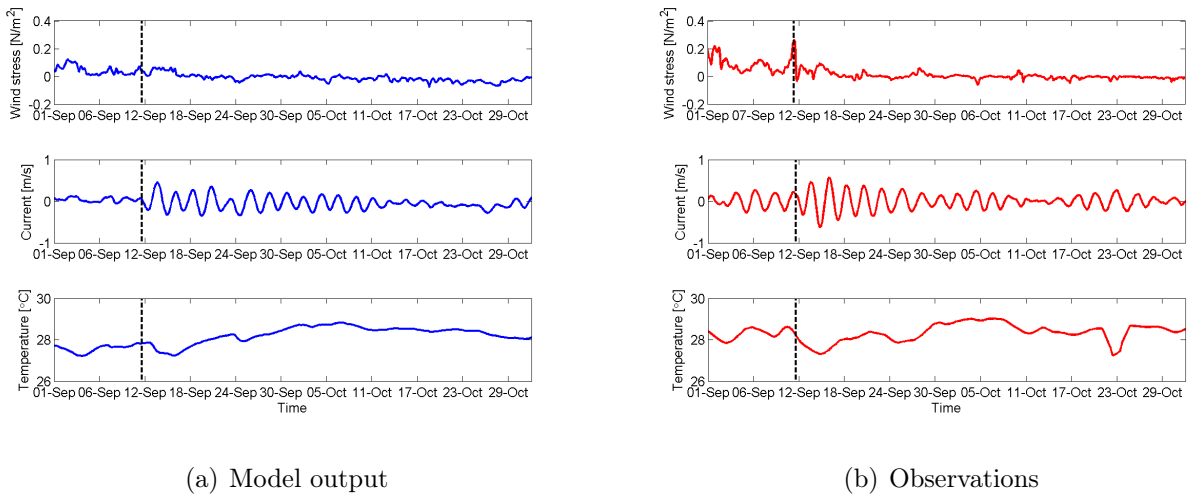
Figure 4.9

The model does not have temperatures in different layers to compare with the observations. Instead the comparison is made with the boundary layer depth, which is shown in figure 4.10, together with the wind stress (above) and the current (below). The black dashed line is the maximum observed zonal wind stress, the black solid line is at the time during the storm where the observations indicate mixing. Due to the mixing seen in the observations a deepening of the boundary layer is expected. The boundary layer depth tends to vary with 10 meters during the time period, so there is no event that stands out as a notable event during the storm, however the deepest boundary layer depth is found at the same time as the observations indicate mixing, which is what was expected. In the observations there were small indications of mixing around the 25 September and 8 October, at these times there seems to be a deepening of the boundary layer, but the events do not stand out as notable events.

Figure 4.11 shows the zonal wind stress, zonal currents and sea surface temperatures for the model (figure 4.11(a)) and observations (figure 4.11(b)) in a comparable plot. The black dashed line is the maximum of the observed zonal wind stress. It is clear that the temperature drops as a result of the increase in wind stress. The currents also increases in amplitude when the wind stress increases. The model output shows a similar behavior to the observations, but the amplitude of the ocean currents is smaller and the notable event (Hurricane Helene) in the wind stress is much smaller in the model output than in the observations.
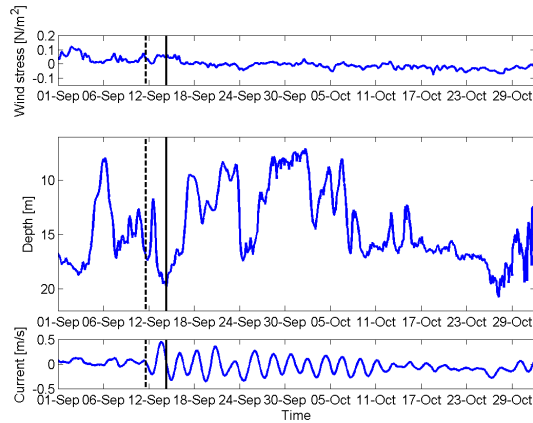
Figure 4.10: The boundary layer depth of the model (middle), the zonal wind stress (upper) and the zonal currents (lower), both of the model as well. The black dashed line indicates where the observed zonal wind stress has its maximum and the black solid line indicates where the observed temperatures indicate mixing during the storm.

(a) Model output

(b) Observations

Figure 4.11: The zonal wind stress (upper), zonal current (middle) and sea surface temperature (bottom) from the (a) model output and (b). The black dashed line indicates where the observed zonal wind stress has its maximum.

It is interesting that the inertial oscillations are notable in the model output, despite the fact that there is no notable hurricane in the model wind stress. This indicates that it indeed is the wind stress that is poorly represented in the model output.

From observations it is clear that Hurricane Helene passes at 12°N 23°W at the 12 September 2006. A method to see if the hurricane is observed in the model is to look at the wind vectors around the known position. The model wind vectors around 12°N 23°W from the 12 September 2006 are shown in figure 4.12, the wind vectors are shown every 4 hours. The rotation of the wind vectors clearly indicates a hurricane rotation. The velocities of the wind vectors are not as strong as expected during a hurricane, but it is clear that a stronger wind field passes at 12°N 23°W around the 12 September, which is consistent with Hurricane Helene.

(a) 12 September 02:00

(b) 12 September 06:00

(c) 12 September 10:00

(d) 12 September 14:00

(e) 12 September 18:00

(f) 12 September 22:00
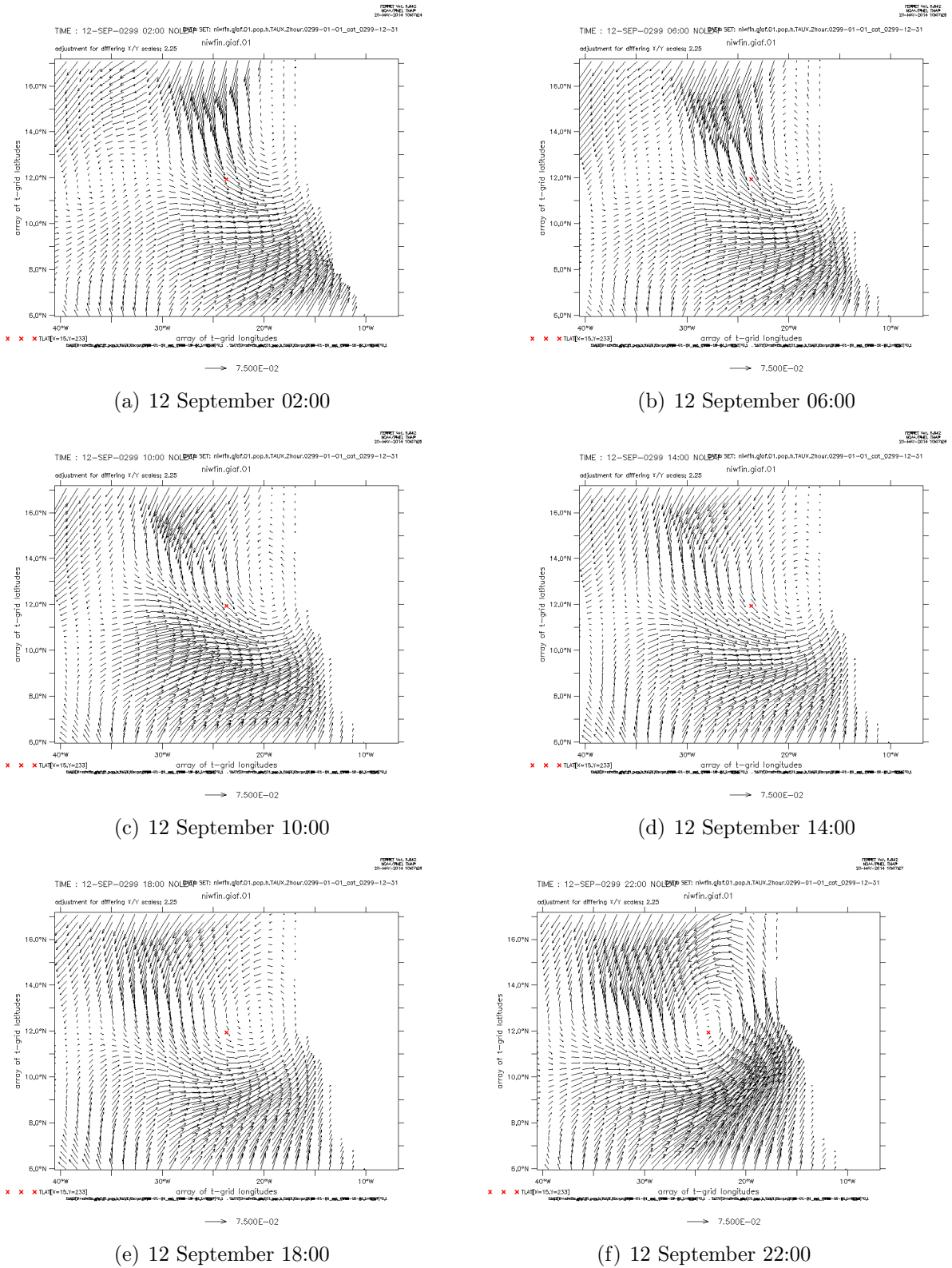
Figure 4.12: The wind vectors from the model output around the 12°N 23°W mooring site (indicated with a red cross). The rotation of the wind vectors definitely indicates a hurricane rotation even though the velocity is very weak.

Looking at the frequency spectrum it is possible to check the performance of the model and see if there is any signal in the near-inertial frequency band. If the wind stress shows a notable peak in the near-inertial frequency band, it indicates near-inertial resonance.

Figure 4.13 shows the zonal (4.13(a)) and meridional (4.13(b)) frequency spectrum for the wind, the blue spectrum is the model data and the red is the observations. The frequency spectrum of the observations is longer (goes to higher frequencies) than the one for the model because the temporal resolution of the spectrum. The temporal resolution of the observations is 10 minutes whereas the temporal resolution of the model is 2 hours. It is possible to resolve much higher frequencies with a 10 minutes resolution than with a 2 hour resolution. It can be seen that the model and the observations generate the same kind of lower frequency variabilities, but then going towards higher frequencies, the frequency variability happening in the model is lower than in the observations. The frequency spectrum of the model output and the observations have about the same variability in the near-inertial frequency band. In the near-inertial frequency band there is no significant peak. Both the model and observations both show a notable peak at the diurnal cycle and at the M2 tide in the zonal direction. In the meridional direction there is no signal in the observations at M2 tide and the signal is very low at the diurnal cycle.

(a)   (b)
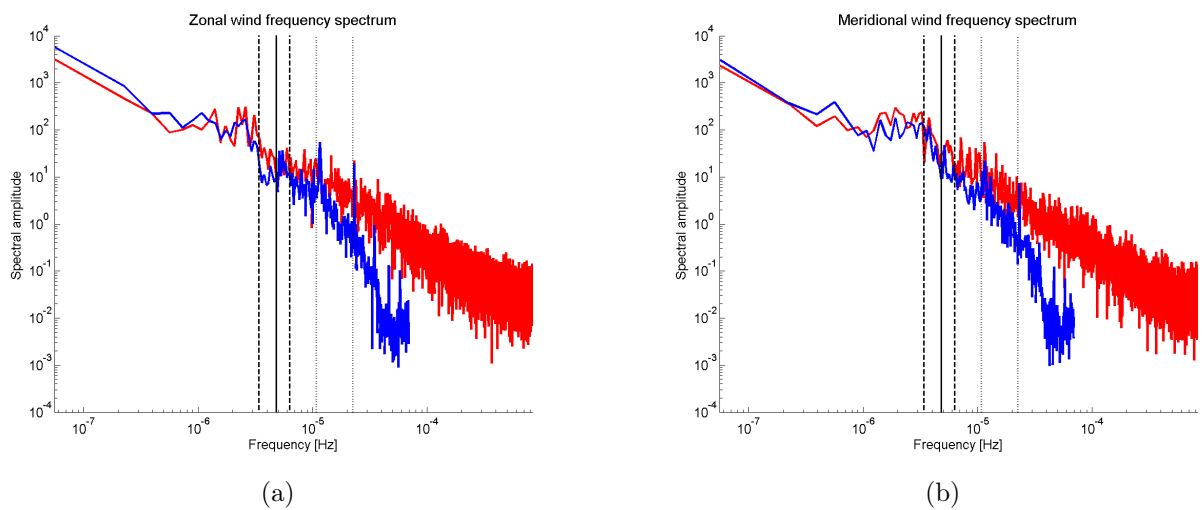
Figure 4.13: The frequency spectra for the wind in the (a) zonal and (b) meridional direction. The black dashed lines indicate the near-inertial frequency band and the black solid line indicates the inertial frequency. The black dotted lines indicate the diurnal cycle and the M2 tide

Figure 4.14 shows the zonal (4.14(a)) and meridional (4.14(b)) frequency spectrum of the current field for the model (blue curve) and observations (red curve). The frequency spectrum of the observations is longer than the one of the model, this is again due to the temporal resolution. The model generally generates lower frequency variabilities than the observations, however, in the near-inertial frequency band the frequency variability is almost the same. Both the model and observations show a distinct peak in the near-inertial frequency band. The model and observations in both directions show a peak at the diurnal cycle and the M2 tide.

(a)   (b)
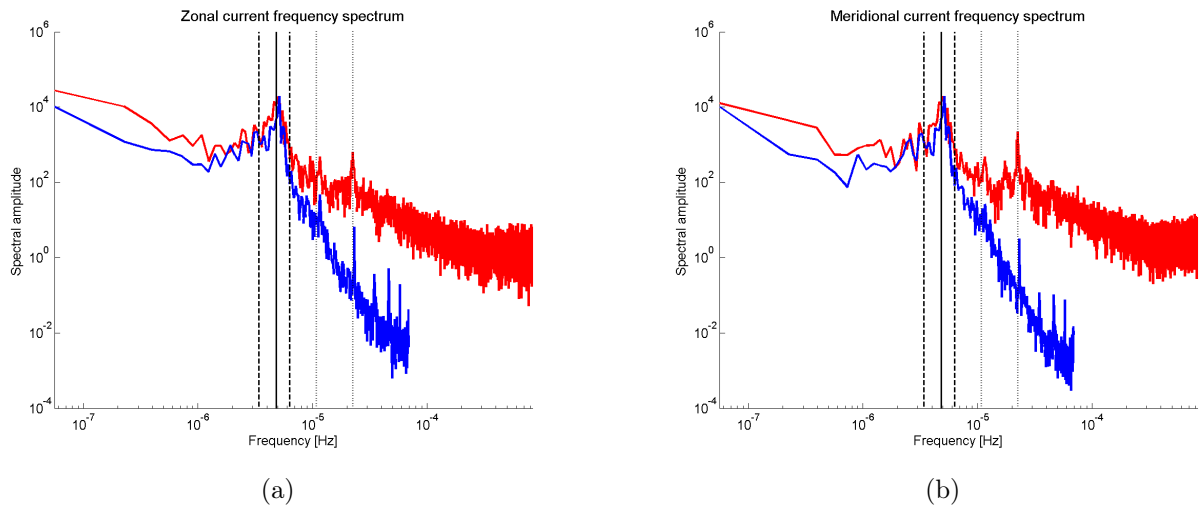
Figure 4.14: The frequency spectra for the currents in the (a) zonal and (b) meridional direction. The black dashed lines indicate the near-inertial frequency band and the black solid line indicates the inertial frequency. The black dotted lines indicate the diurnal cycle and the M2 tide.

4.2 Model/observation comparison of wind/near-inertial waves at $4°N$ $23°W$

In order to compare the model with the observations of the interaction between the wind and the near-inertial waves throughout the seasonal cycle data from a full year is needed. The time period used in the comparison at $4°N$ $23°W$ is from 1 January 2008 at 02:00 to 31 December 2008 at 22:00.

Figure 4.15 shows the zonal (4.15(a)) and meridional (4.15(b)) wind stress of the model (blue lines) and the observations (red curve). Here it can be seen that the model and observations have a similar behavior over the seasonal cycle. The amplitude of the wind stress of the model is larger than the amplitude of the wind stress of the observations. The flow of the wind stress is even through the year. Around the 1 June 2008, the wind stress in the meridional direction becomes 0.05 N/m^2 higher and starts varying with about 0.15 N/m^2 instead of 0.08 N/m^2 for the model and 0.1 instead of 0.05 for the observations. In the zonal direction the wind stress is approximately the same over the year, the variation of the wind stress is approximately the same as well (about 0.1 N/m^2 for the model and 0.07 N/m^2 for the observations).

(a)   (b)
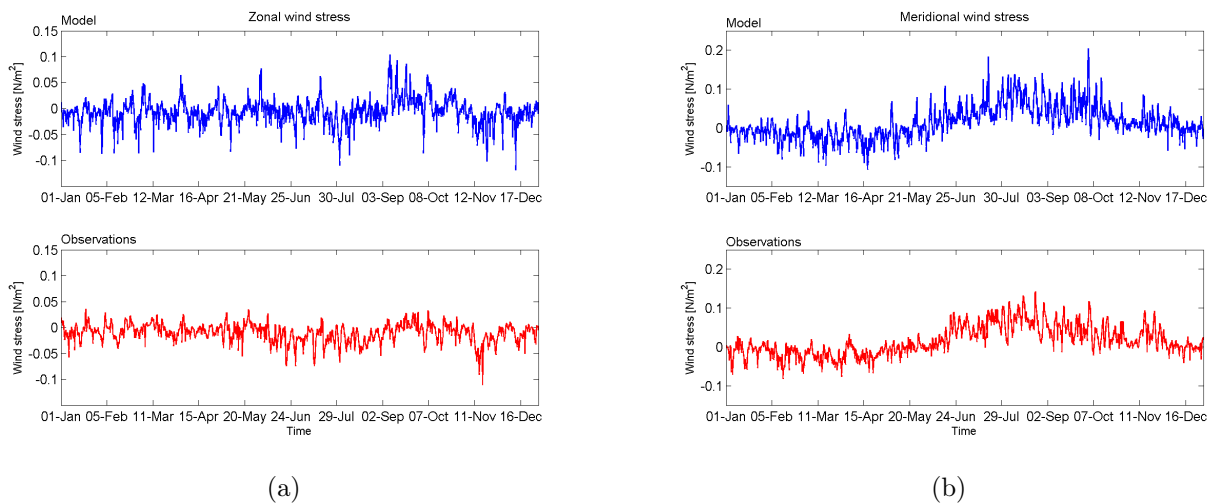
Figure 4.15: The (a) zonal and (b) meridional wind stress of the model (blue curve) and the observations (red curve).

Figure 4.16 shows the zonal (4.16(a)) and meridional (4.16(b)) currents for the model (blue curves) and observation (red curves). The currents are not as similar as the wind stresses. In the zonal direction the model currents have a similar behavior to the currents from the observations, but it is a bit delayed and the currents are a little to high in the oscillations that happen from 20 May 2008 to 1 November. The decrease followed by a sudden increase in the observations around the 8 December is not reproduced by the model. In the meridional direction, the model currents are similar to the observations, but

all peaks in the observations are not reproduced by the model. The model does not seem to simulate the currents correctly here. The general behavior is the same, but there are several distinct features the model does not reproduce.

(a)   (b)
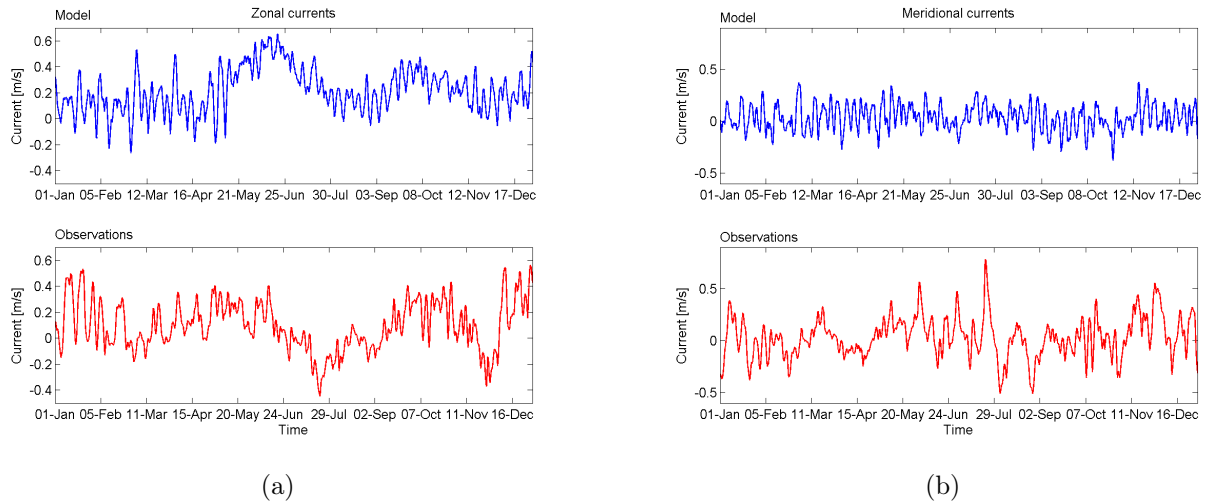
Figure 4.16: The (a) zonal and (b) meridional currents of the model (blue curve) and the observations (red curve).

The annual mean near-inertial velocity is calculated by the two methods explained in section 2.4. The results are shown in table 4.3, with $|U_{NI}|$ as the results of the Butterworth bandpass filter method and σ_{NI} as the result of the near-inertial variance method. It is clear that the model performs well in calculating the annual mean near-inertial velocity. The model annual mean near-inertial velocity is a little higher than the observed near-inertial velocity.

	Model	Observations
σ_{NI}	13.74 cm/s	12.14 cm/s
$|U_{NI}|$	10.37 cm/s	9.97 cm/s

Table 4.3: The mean near-inertial velocity for the year at 4°N found by two methods, $|U_{NI}|$ being the Butterworth bandpass filter method and σ_{NI} being the near-inertial variance method.

Figure 4.17 shows a histogram of the near-inertial velocities, found by the Butterworth bandpass filter method, for the model (4.17(a)) and observations (4.17(b)). The black line shows the annual mean near-inertial velocity. It can be seen that the model and observed data are very similar in where the near-inertial velocities comes from. None have values higher than 0.3 m/s and both have highest distribution of counts at values a little smaller than the mean near-inertial velocity (values of 0.08 m/s for the model and 0.065 for the observations).

(a) Model
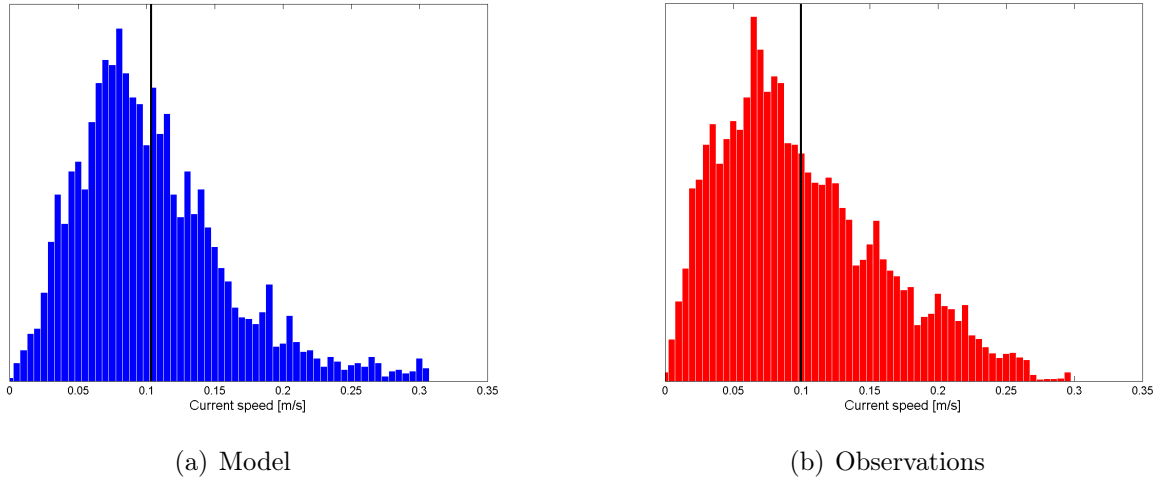
(b) Observations

Figure 4.17: Histogram of the near-inertial velocities of the (a) model and (b) observations. The black line indicates the mean near-inertial velocity of the time period.

The near-inertial frequency band at 4°N 23°W is shown in table 4.4. The diurnal cycle is expected at $\frac{1}{24\text{h}} = \frac{1}{86400\text{s}} = 1.16 \cdot 10^{-5}$ Hz and the M2 tide (the semidiurnal cycle) is expected at $\frac{1}{12\text{h}} = \frac{1}{43200\text{s}} = 2.31 \cdot 10^{-5}$ Hz.

$0.7f_i$	f_i	$1.3f_i$
$1.13 \cdot 10^{-6}$ Hz	$1.62 \cdot 10^{-6}$ Hz	$2.10 \cdot 10^{-6}$ Hz

Table 4.4: The near-inertial frequency band is located between $0.7f_i$ and $1.3f_i$, where $f_i = 2\omega \sin(\phi)$. At 4°N the near-inertial band is located at these values.

Figure 4.18 shows the zonal (4.18(a)) and meridional (4.18(b)) frequency spectrum of the wind stress for the model (blue spectrum) and the observations (red spectrum). The frequency spectrum for the observations is longer than the one of the model, this is due to the higher temporal resolution for the observations than for the model. The model and observations generate the same kind of lower frequency variability, but as the frequencies become higher and reach $2 \cdot 10^{-5}$ Hz, the frequency variabilities happening in the model are not as high as the frequency variabilities of the observations. There is no signal in the near-inertial frequency band. The diurnal cycle and the M2 tide are both clear in the model spectrum, but not visible in the observations.

(a)

(b)
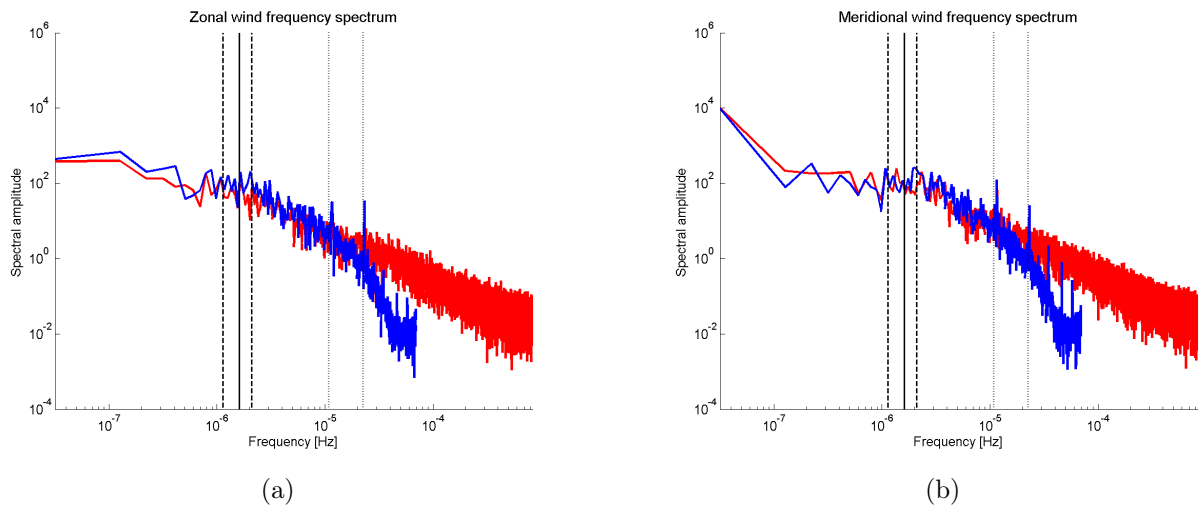
Figure 4.18: The (a) zonal and (b) meridional frequency spectrum for the wind. The black dotted lines indicate the diurnal cycle and the M2 tide, the black dashed lines indicate the near-inertial frequency band and the black solid line indicates the inertial frequency.

Figure 4.19 shows the zonal (4.19(a)) and meridional (4.19(b)) frequency spectrum of the currents of the model (blue spectrum) and observations (red spectrum). The frequency spectrum of the observations is longer than the one for the model due to the temporal resolutions. It can be seen that the model generates generally a lower frequency variability than the observations. In the near-inertial frequency band the frequency spectrum of the model and the observations have approximately the same variability. In the zonal direction the frequency spectrum of the model and observations generate the same kind of frequency variability at very low frequencies, whereas the model generates lower frequency variabilities than the observations from the beginning of the frequency spectrum in the meridional direction. There is a little peak in the near-inertial frequency band, and there is a notable peak at the diurnal cycle and at the M2 tide in both directions.


(a)

(b)
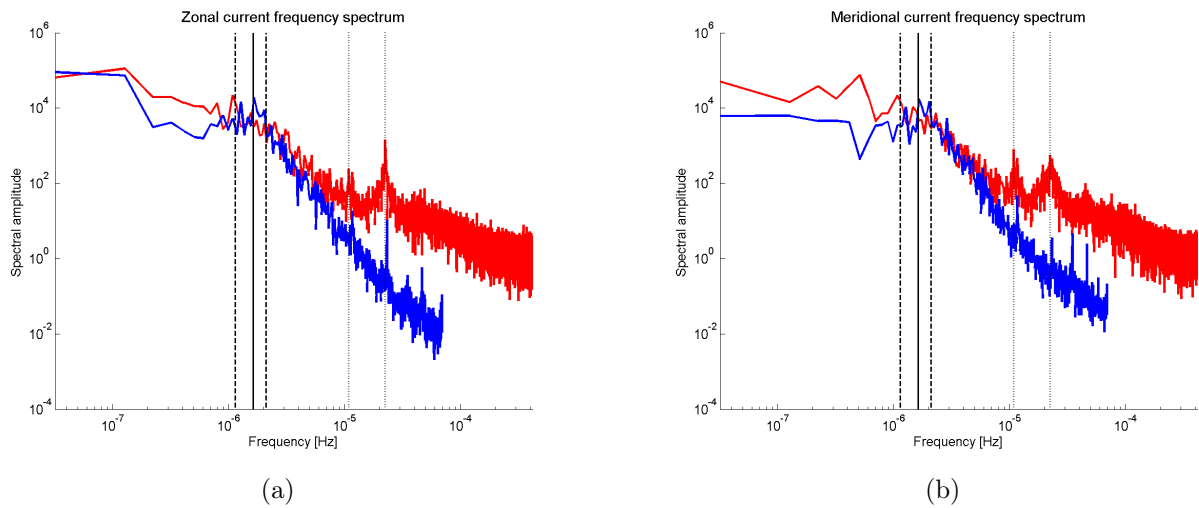
Figure 4.19: The (a) zonal and (b) meridional frequency spectrum for the currents. The black dotted lines indicate the diurnal cycle and the M2 tide, the black dashed lines indicate the near-inertial frequency band and the black solid line indicates the inertial frequency.

## 4.3 Model/observation comparison of wind/near inertial waves at $12°N$ $23°W$

The interaction between wind and near-inertial waves at $12°N$ $23°W$ is based on data in the period from 8 June 2006 at 16:00 to 3 May 2007 at 18:00.

Figure 4.20 shows the zonal (4.20(a)) and meridional (4.20(b)) wind stress for the model (blue lines) and the observations (red lines). It can be seen that the model and observations have a similar behavior in both directions. The wind stress of the observations is larger than the wind stress of the model. In the zonal direction the model flow varies by 0.05 N/m^2 and the observed flow by 0.09 N/m^2 around 0 N/m^2 until 24 September, where it decreases to vary around -0.05 N/m^2, the model still by 0.05 N/m^2 and the observations by 0.08 N/m^2. In the meridional direction the flow varies around 0 N/m^2, the model by 0.05 N/m^2 and the observations by 0.1 N/m^2 until 24 September, where it decreases to vary around -0.05 N/m^2 still by 0.05 N/m^2 for the model and the observations by 0.08 N/m^2.

(a)   (b)
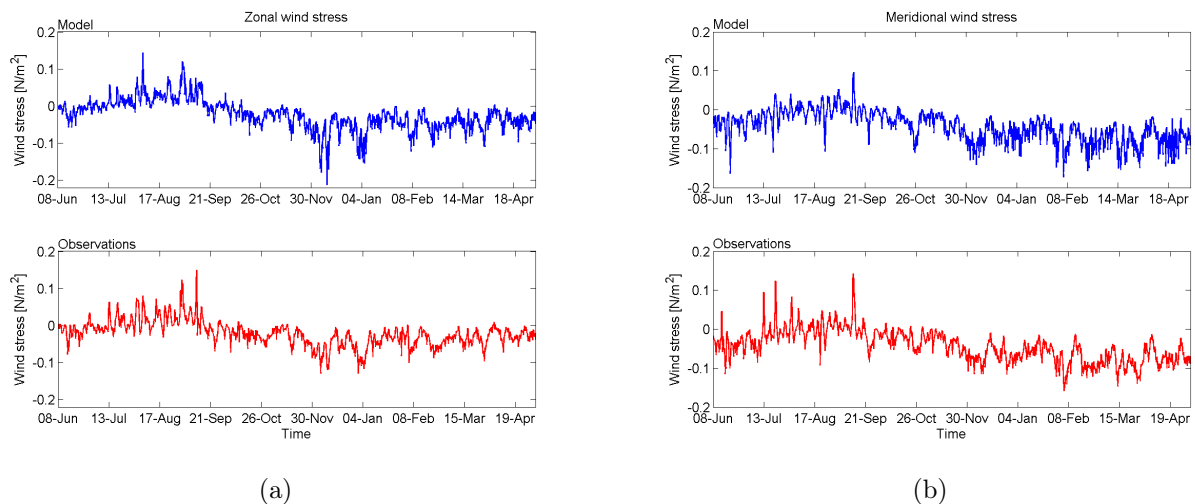
Figure 4.20: The (a) zonal and (b) meridional wind stress of the model (blue curve) and the observations (red curve).

Figure 4.21 shows the zonal (4.21(a)) and meridional (4.21(b)) currents for the model (blue lines) and observations (red lines). It can be seen that the model follows the observed data. The events that happen in the period are simulated the model, but the features start later in the model output than they do in the observations. For instance the large event around the 15 September starts with increased currents at the 3 September in the observations, whereas the currents in the model not increase until the 13 September in both directions. The amplitude of the events are also higher in the observations than in the model. The amplitude of the zonal current is 1.20 m/s in the observations and 0.63 m/s in the model. In the meridional direction the amplitude of the observations is 1.10 m/s whereas the model amplitude is 0.64 m/s.
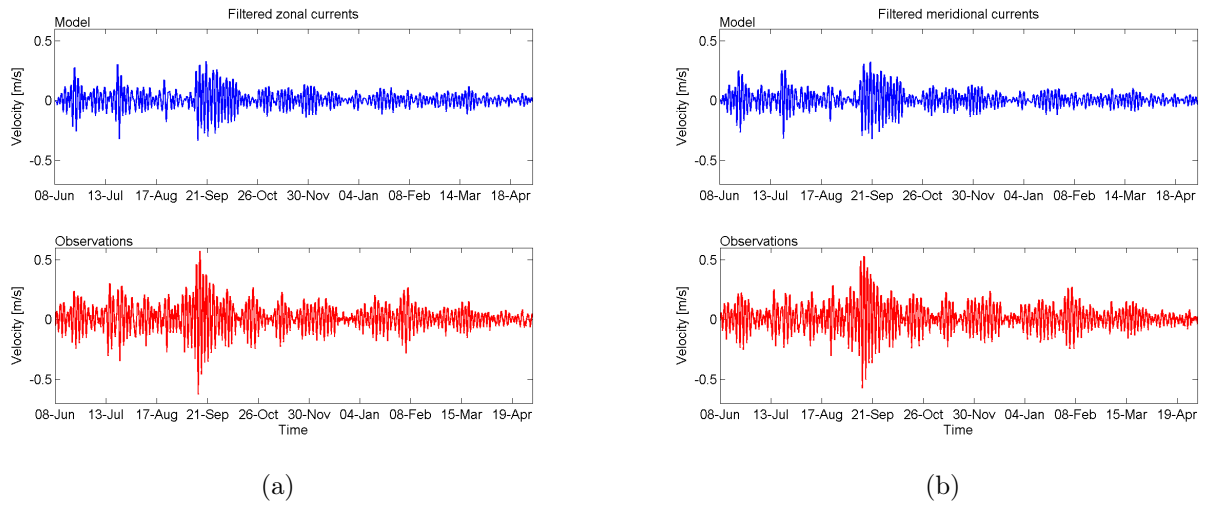
Figure 4.21: The (a) zonal and (b) meridional currents of the model (blue curve) and the observations (red curve).

The annual mean near-inertial velocity over the time period is calculated by the two methods explained in section 2.4. The results are shown in table 4.5, with $|U_{NI}|$ as the results of the Butterworth bandpass filter method and σ_{NI} as the result of the near-inertial variance method. It can be seen that the model does not perform as well at 12°N as it did at 4°N. The annual mean near-inertial velocity calculated from the model data is approximately 2/3 of the annual mean near-inertial velocity from the observed data.

	Model	Observations
σ_{NI}	11.06 cm/s	16.54 cm/s
$|U_{NI}|$	8.54 cm/s	12.92 cm/s

Table 4.5: The mean near-inertial velocity over the time period at 12°N found by two methods, $|U_{NI}|$ being the result of the Butterworth bandpass filter method and σ_{NI} being the result of the near-inertial variance method.

Figure 4.22 shows a histogram of the Butterworth bandpass filter method near-inertial velocities for the model (4.22(a)) and observations (4.22(b)). The black line indicates the mean near-inertial velocity over the time period. It can be seen, that the model does not have any high events contributing to the near-inertial velocities, no events higher than 0.335 m/s, whereas the observations have some high events contributing, the highest events in the observations are 0.665 m/s.

(a) Model
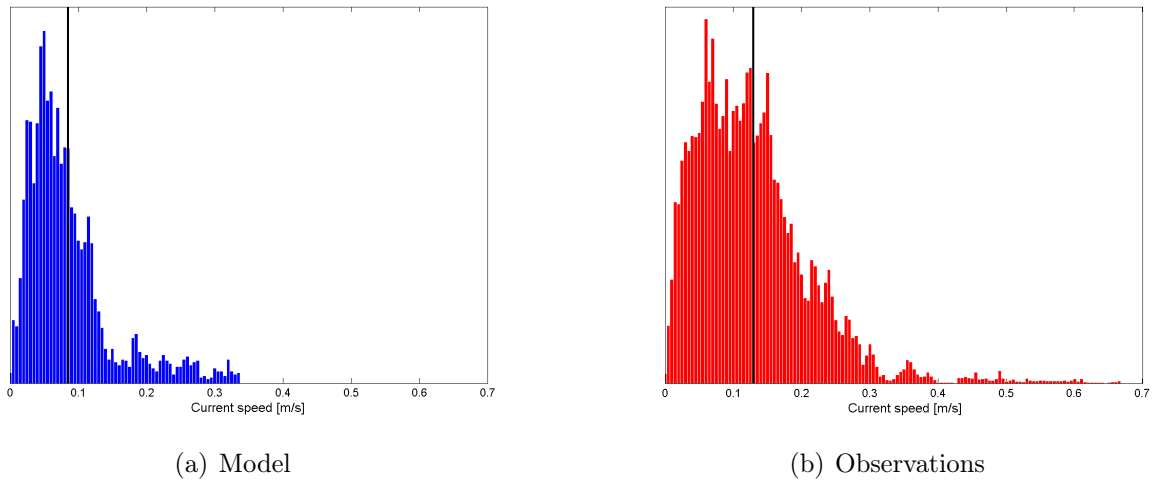
(b) Observations

Figure 4.22: Histogram of the near-inertial velocities of the (a) model and (b) observations. The black line indicates the mean near-inertial velocity of the time period.

Inertial motions are expected in the near-inertial frequency band (between $0.7f_I$ and $1.3f_I$), which at 12°N 23°W is between the values shown in table 4.2. The diurnal cycle and the M2 tide are located at the same frequencies at all locations, which is at $\frac{1}{24\text{h}} = \frac{1}{86400\text{s}} = 1.16 \cdot 10^{-5}$ Hz and $\frac{1}{12\text{h}} = \frac{1}{43200\text{s}} = 2.31 \cdot 10^{-5}$ Hz respectively.

Figure 4.23 shows the frequency spectrum for zonal (4.23(a)) and meridional (4.23(b)) wind stress for the model (blue spectrum) and the observations (red spectrum). The frequency spectrum of the observations is longer than the one for the model due to the temporal resolutions. It can be seen that the model and observations generate the same kind of lower frequency variabilities, but going towards higher frequencies, the frequency variability happening in the model is lower than the one of the observations. There is no notable peak in the near-inertial frequency band in either direction. In the zonal direction the model and the observational output both show a notable peak at the diurnal cycle and at M2 tide. In the meridional direction the spectral frequencies of the observations show a notable peak at the diurnal cycle and M2 tide, whereas the model output only shows a notable peak at the diurnal cycle and at M2 tide the peak is not as significant.
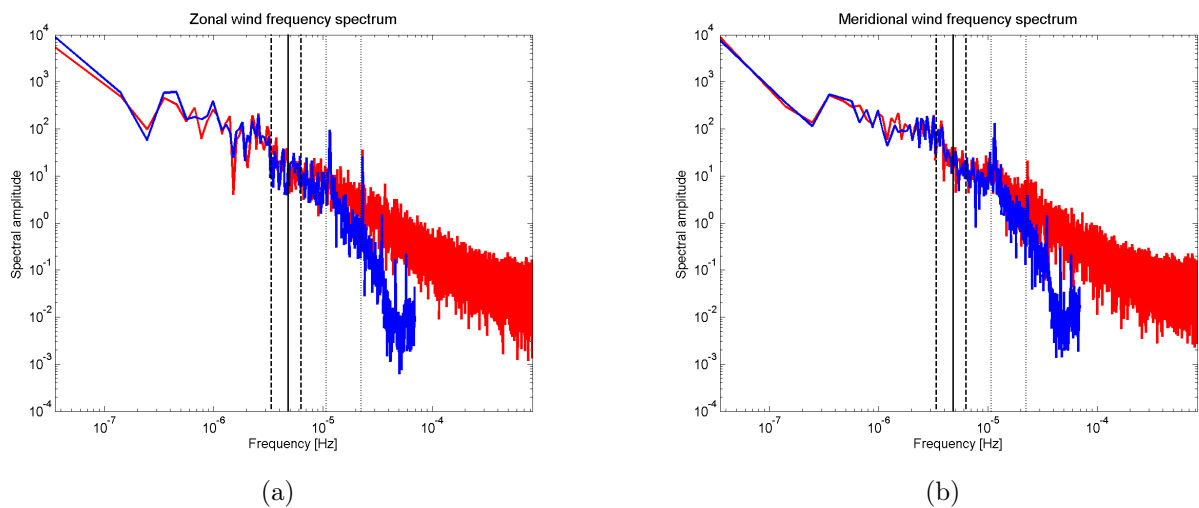
Figure 4.23: The (a) zonal and (b) meridional frequency spectrum for the wind. The black dashed lines indicate the near-inertial frequency band and the black solid line indicates the inertial frequency. The black dotted lines indicate the diurnal cycle and the M2 tide

Figure 4.24 shows the zonal (4.24(a)) and meridional (4.24(b)) frequency current spectrum for the model (blue spectrum) and the observations (red spectrum). The frequency spectrum of the observations is longer than the one for the model due to the temporal resolutions. It is clear that at low frequencies the model and the observations generate the same kind of variabilities, going towards higher frequencies, however, the frequency variability happening in the model is lower than the one happening in the observations. The frequency spectrum of the model output and the observations have about the same variability in the near-inertial frequency band. Both the model and the observations show a notable peak in the near-inertial frequency band. There is also a clear peak at the diurnal cycle and M2 tide in both directions.
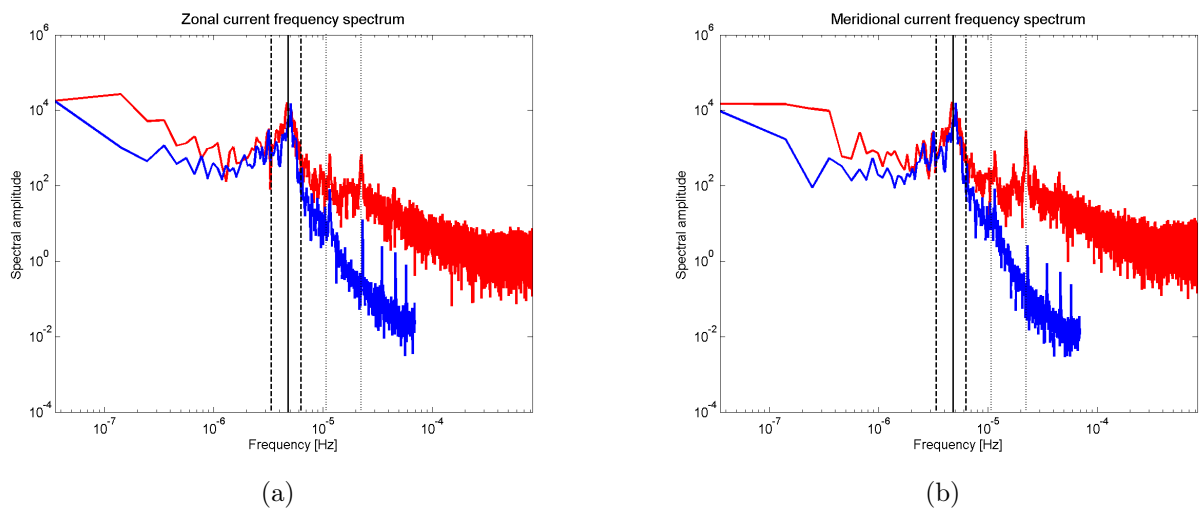
Figure 4.24: The (a) zonal and (b) meridional frequency spectrum for the current. The black dashed lines indicate the near-inertial frequency band and the black solid line indicates the inertial frequency. The black dotted lines indicate the diurnal cycle and the M2 tide.

5 Discussion

The key question of this thesis is to understand the specific role of near inertial waves and the driving of vertical mixing. This chapter will discuss the findings during the work with this thesis and compare it to previous efforts.

Near-inertial velocities

According to Elipot et al. (2010) the near-inertial variance of the near-inertial waves equals the kinetic energy in the near-inertial frequency band. The velocity of the near-inertial waves can therefore be gained by this variance (the near-inertial variance method, explained in section 2.4.1) or using filtration (Butterworth bandpass filter method, section 2.4.2).

The near-inertial velocities are found using the two methods and compared to previous studies. Table 5.1 shows the near-inertial velocities found in the work with this thesis (represented as $|U_{NI}|$ and σ^2_{NI}) compared to previous efforts.

	Elipot & Lumpkin (2008)	Elipot et al. (2010)
4°N 23°W	15.0 cm/s [10 cm/s; 25.5 cm/s]	-
12°N 23°W	13.8 cm/s [8.7 cm/s; 30.0 cm/s]	15.8 cm/s
	Chaigneau et al. (2008)	Jochum et al. (2013)
4°N 23°W	≈ 10 cm/s	11-13 cm/s
12°N 23°W	≈ 20 cm/s	7-10 cm/s
	$|U_{NI,obs}|$	$\sigma^2_{NI,obs}$
4°N 23°W	9.97 cm/s	12.14 cm/s
12°N 23°W	12.92 cm/s	16.54 cm/s
	$|U_{NI,model}|$	$\sigma^2_{NI,model}$
4°N 23°W	10.37 cm/s	13.74 cm/s
12°N 23°W	8.54 cm/s	11.06 cm/s

Table 5.1: Near-inertial velocities at the two mooring locations found by different authors and with different methods. The brackets in the results from Elipot & Lumpkin (2008) indicates the uncertainty range of the results.

The differences in the results are most likely caused by differences in the spatial and temporal resolution of the studies and which method is used in the collection of data. Elipot & Lumpkin (2008) uses drifter-buoys with the position of the buoys divided into latitude bands of 2.5°. Elipot et al. (2010) is also a drifter-buoy study, but with a spatial resolution of 1°. Chaigneau et al. (2008) uses satellite-tracked surface drifter data with a spatial resolution of 2°. Jochum et al. (2013) uses the CCSM4 with a spatial resolution of 1.125° in longitude and varying in the latitude from 0.27° at the equator to approximately 0.7° at high latitudes.

The near-inertial velocities for the mooring data from this thesis are most comparable with Elipot et al. (2010), since this is a study based on observed data and the study with the highest spatial resolution. However, the results of this study do not extend down to the 4°N 23°W mooring and therefore it is not possible to compare this mooring with the Elipot et al. (2010) study. Elipot & Lumpkin (2008) and Chaigneau et al. (2008) are also studies based on observational data and therefore comparable with the mooring data. Elipot & Lumpkin (2008) extends all the way through equator and is therefore the best study to compare the 4°N 23°W mooring to. The study by Jochum et al. (2013) is based on the CCSM4 model and is therefore the best study to compare the model data in this thesis with.
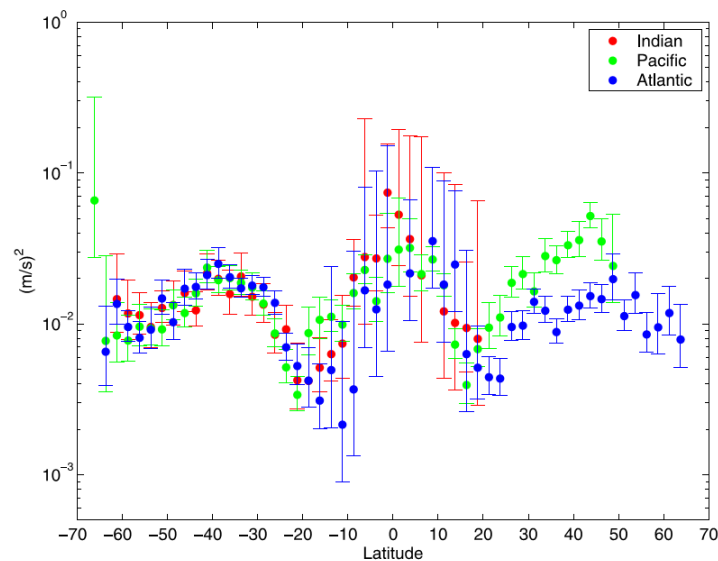
Figure 5.1: The near-inertial velocities found by Elipot & Lumpkin (2008).

It is clear, that averaged over a year, the model compares well to the observations when it comes to simulating near-inertial velocities. The results are inside the range of uncertainty determined by Elipot & Lumpkin (2008) shown in figure 5.1 (represented inside the square brackets in table 5.1).

The temporal resolution of models and observations can also have effect on how well the currents are resolved. Figure 5.2 shows an example of how a wave can change just by changing the temporal resolution. The blue curve is the near-inertial waves from 12°N with

the temporal resolution of 10 minutes, the red curve shows the same near-inertial waves with the temporal resolution of 2 hours. It is clear that with a high temporal resolution it is possible to see the most precise movement of the oceanic waves. Having a lower temporal resolution can distort the current movement.
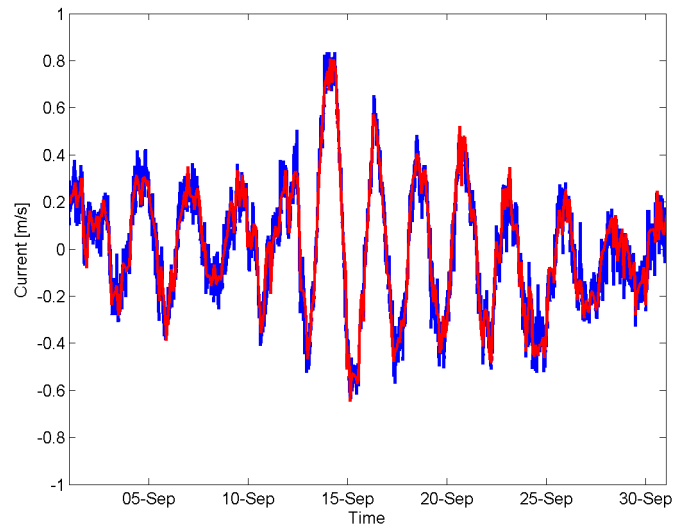
Figure 5.2: A comparison of temporal resolutions. The blue curve show near-inertial waves from the 12°N mooring with a temporal resolution of 10 minutes and the red curve shows the same near-inertial waves with a temporal resolution of 2 hours.

Rimac et al. (2013) found that near-inertial motions care more about how often the winds blow over the ocean rather than the spatial resolution. If the resolution of the atmosphere is made coarser, this does not change to much, but if the time is changed, such that the oceans feel the winds blowing less often, this tends to really affect the near-inertial activities.

Mixed layer depths

A case study of the Hurricane Helene is made to examine the response of the mixed layer to a hurricane and to examine how well the model resolves a hurricane. Ideally this study is performed by looking at the heat redistribution through the mixed layer and the layer below. This is done for the observations by looking at the temperatures in 12 different depths ranging from the sea surface down to 500 meters. The model output unfortunately only has the sea surface temperature, and therefore it is not possible to look at the temperatures through the layers here. Instead the boundary layer depth is used for the model output. This will not give the same overview of how the model resolves the mixing through the layers, which would have been preferable for the purpose of the thesis.

It was clear, when looking at the model output for the wind stress, figure 4.2, that Hurricane Helene would not have been classified as a hurricane in the model output. The

winds have the rotation of a hurricane (figure 4.12), but the model does not resolve them strong enough.

In figure 4.6 clear indications of a mixing in the upper ocean are seen. At the time of the hurricane the sea surface temperature, as well as the temperature in 10 and 13 meters depth, are decreasing, while the temperature in 20 meters depth is increasing. It is searched for this in the boundary layer depth of the model output, expecting a deepening of the boundary layer. The deepest boundary layer depth is actually at the same time as the observed mixing, but the variations in the boundary layer are in order of 10 meters during the whole time period, so this does not stand alone as a notable event. The upper-ocean mixing events found in the observations later in the time series (26 September and 8 October) also seem to be reproduced by the model. But, again, they do not stand out as notable events and it is therefore uncertain if it is caused by the observed mixing.

However, even though the wind seems to be poorly resolved in the model output, it looks like the model reproduces the near-inertial waves. Hence the variabilities in the boundary layer depth can be caused by these near-inertial waves.

Dohan & Davis (2011) uses data from an array of moorings to examine the storm-driven upper-ocean evolution during two autumn storms of comparable magnitude, but with very different responses in the upper ocean. The mixed layer depth in the first storm deepens as in the fashion normally seen in storms. The mixed layer depth in the second storm does not deepen, instead the transition layer below does. Dohan & Davis (2011) conclude, that the turning of the winds in the second storm are resonating, exciting the oceans and creating near-inertial oscillations. These oscillations then propagate out of the mixed layer.

Unfortunately this thesis does not find resonating turning in the winds during the passage of the storm. Therefore the results of Dohan & Davis (2011) are not reproduced in this thesis.

Model versus observations

Comparing the near-inertial velocities found in current study with mooring data and model data, it is possible to determine the performance of the model. It is clear, that the model performs better at 4°N 23°W than at 12°N 23°W. At 4°N 23°W the model determines the near-inertial velocities to be slightly higher than the one of the mooring data, whereas the model at 12°N 23°W determines near-inertial velocities that are 2/3 of the near-inertial velocities of the mooring data. This is explained by Jochum et al. (2013) to be due to the effect of the Coriolis force. Going further North the Coriolis force, f, becomes stronger and tropical storms narrower. Hurricanes are for instance much bigger than midlatitude storms. This means that it is much easier to resolve atmospheric motions near the equator, which means that the model resolution in high resolution often is to coarse to resolve these storms in spite of being the same as at equator. On the other hand, the closer to equator, the bigger the features become and the easier it is for the model to resolve them.

It is shown that the model performs reasonable when it comes to simulate the annual average of the near-inertial velocities, but when it comes to a specific storm event, the winds are poorly resolved.

Even though the model resolves the winds poorly, it actually resolves the near-inertial waves. Though the amplitude of the near-inertial waves are to small compared to the observed data, which can be caused by the grid resolution of the model. With a grid resolution of 1° the model can not resolve small features moving inside the grid boxes, whereas a mooring observes passing features with a high accuracy.

The model performs perfectly in resolving the period of the inertial waves. An example of this is figure 4.3, which is the plot of the current velocities at 12°N 23°W. Here it is clear, that the period of the model output is perfectly equal to the one of the mooring output.

6 Conclusion

The main motivation of this thesis was to understand the specific role of near inertial waves in the oceans and the driving of vertical mixing. Inertial waves play an important role in the climate, but their importance is not fully understood yet since they are not fully resolved in climate models. Therefore one of the main purposes of this thesis was to determine how well the CESM forced simulation resolves near-inertial waves, by looking at mixing in the upper ocean, since near-inertial waves are proven to affect the deepening of the ocean mixed layer (Dohan & Davis, 2011) and near-inertial velocities.

The annual mean near-inertial velocity is examined by using mooring data from two different sites (4°N 23°W and 12°N 23°W) and the CESM forced simulation. The annual mean near-inertial velocity is found using two different methods: the near-inertial variance method, determining the variance of the near-inertial spectral band, and the Butterworth bandpass filter method, filtering the current time series in the near-inertial frequency band. The model performs well in determining the annual mean near-inertial velocities using both methods. The near-inertial velocities, computed from the model output, are quite similar to the near-inertial velocities computed from the mooring data. The annual mean near-inertial velocities are found within the near-inertial velocity range of the uncertainties determined by Elipot & Lumpkin (2008), and they are of comparable strength to the three other studies (Elipot et al. (2010), Chaigneau et al. (2008) and Jochum et al. (2013)) used for comparison in the discussion.

The ocean's response to the Hurricane Helene has been examined using mooring data from the 12°N 23°W site and the CESM forced simulation. The observational data of Hurricane Helene shows sea surface cooling and heating of the lower level temperature at 20 meters depth, which is a clear indication of mixing. Additionally the mooring data show that during Hurricane Helene there is an enhancement of inertial oscillations throughout the mixed layer and the transition layer below. Resonant turning in the winds is not found during the passage of Hurricane Helene, which means that the results of Dohan & Davis (2011) are not reproduced. This case study of Hurricane Helene is made to examine how well the model performs when it comes to a specific storm event. It is found that the model simulates the near-inertial waves, but performs poorly in resolving the winds. The boundary layer depth shows indications of a deepening of the boundary layer in the time periods where the observations indicate mixing. This was expected, but the results are not convincing since the boundary layer depth varies with approximately 10 meters during the entire time period. If the variations seen in the boundary layer depth actually

are caused by mixing, due to the inertial waves and the varying after the storm might be some kind of ringing, or if they are the normal diurnal cycle of the boundary layer is not conclusively determined. It is not convincing to determine when the wind is so poorly resolved. Even though the model is forced by observed winds it does not seem like the atmospheric component of the CESM forced simulation contains hurricanes.

The key results of this thesis is that looking over an annual time series the estimates of the average inertial wave current speed are consistent with previously published modeling and observational efforts. Looking at a single storm event, however, the model does not perform very well. The problem is probably that the atmospheric resolution of the model is to coarse in both time and space.

6.1   Further work

During the work with this thesis it would have been very interesting to compare the temperatures of the model output and observational data throughout the mixed layer and the layer below. This would be interesting since it could give a better understanding of how well the near-inertial waves are resolved throughout the uppermost layers in the model. This was not possible since the sea surface temperature was the only saved temperature in the CESM forced simulation. It is therefore suggested that the temperature in different depths are saved and this comparison is made.

It is concluded in this thesis that the winds are poorly resolved in the model. This can be caused by the spatial and temporal resolution of the atmospheric component of the model. It could therefore be interesting to investigate if it would improve the simulated winds if the forced simulation was run with a higher spatial and temporal resolution of the atmosphere.

It would have been interesting to find resonating winds during the passage of Hurricane Helene in order to make an effort to reproduce the results of the paper by Dohan & Davis (2011). This was unfortunately unsuccessful, since the winds do not turn at resonating frequencies. It would be interesting to find resonating winds during the passage of a hurricane or strong wind field and try to reproduce the results from Dohan & Davis (2011).

Acknowledgments

First of all I would like to thank my supervisor Marcus Jochum for inspiring me to do this study, for the guidance and talks along the way and for helping me to understand the theory.

A big thanks to Brian Sørensen for helping me with installing Linux on my secondary computer. This made it possible for me to receive data from the model, using the server and Ferret. During the process he also helped me to understanding the language of Linux. Brian has also helped with problems in Matlab and with theoretical knowledge along the way. Also thank you Hannah Kleppin for helping me to install Ferret and learn to use it, and Jonas Blüdgen Sølvsteen for helping me with Matlab, Ferret and Latex problems during the last year.

Thank you Helen Pillar for giving me a lot of good advises and help during the writing of the thesis and for proofreading the thesis. Also Johanne Aagaard and Iben Koldtoft for proofreading my thesis and for some good lunch breaks during the last year.

Also a big thank you to all of you at the office for positivity and feedback every time I needed help regardless if it was for Matlab/Ferret/Latex problems or problems with the basic theory along the way.

Finally I would like to thank my family for being there even though I have been "unavailable" the last couple of months.

Turid Lakså

Bibliography

Aldridge, K. D. & Lumb, L. I. (1987). Inertial waves identified in the Earth's fluid outer core. *Nature*, 325, 421–423.

Alford, M. H., Cronin, M. F., & Klymak, J. M. (2012). Annual Cycle and Depth Penetration of Wind-Generated Near-Inertial Internal Waves at Ocean Station Papa in the Northeast Pacific. *Journal of Physical Oceanography*, 42, 889–909. doi: 10.1175/JPO-D-11-092.1.

Alford, M. H., Shcherbina, A. Y., & Gregg, M. C. (2013). Observations of Near-Inertial Internal Gravity Waves Radiating from a Frontal Jet. *Journal of Physical Oceanography*, 43, 1225–1239. doi: 10.1175/JPO-D-12-0146.1.

Apel, J. R. (1988). *Principles of Ocean Physics*, volume 38 of *International Geophysics Series*. Academic Press.

Bourles, B., Lumpkin, R., McPhaden, M. J., Hernandez, F., Nobre, P., Campos, E., Yu, L., Planton, S., Busalacchi, A., Moura, A. D., Servain, J., & Trotte, J. (2008). THE PIRATA PROGRAM: History, Accomplishments, and Future Directions. *Bulletin of the American Meteorological Society*, 89, 1111–1125.

Brown, D. P. (2007). *Hurricane Helene*. Tropical Cyclone Report http://www.nhc.noaa.gov/2006atlan.shtml, National Hurricane Center.

Chaigneau, A., Pizarro, O., & Rojas, W. (2008). Global climatology of near-inertial current characteristics from Lagrangian observations. *Geophysical Research Letters*, 35(L13603), 1–5. doi: 10.1029/2008GL034060.

Danabasoglu, G., Bates, S. C., Briegleb, B. P., Jayne, S. R., Jochum, M., Large, W. G., Peacock, S., & Yeager, S. G. (2012). The CCSM4 Ocean Component. *Journal of Climate*, 25, 1361–1389.

Danabasoglu, G., Large, W. D., Tribbia, J. J., Gent, P. R., Briegleb, B. P., & McWilliams, J. C. (2006). Diurnal Coupling in the Tropical Oceans of CCSM3. *Journal of Climate*, 19, 2347–2365.

D'Asaro, E. A. (1985). The Energy Flux from the Wind to Near-Inertial Motions in the Surface Mixed Layer. *Journal of Physical Oceanography*, 15, 1043–1059.

D'Asaro, E. A. (1995a). A Collection of Papers in the Ocean Storms Experiment - An Introduction. *Journal of Physical Oceanography*, 25, 2817–2818.

D'Asaro, E. A. (1995b). Upper-Ocean Inertial Currents Forced by a Strong Storm. Part II: Modeling. *Journal of Physical Oceanography*, 25, 2937–2952.

D'Asaro, E. A. (1995c). Upper-Ocean Inertial Currents Forced by a Strong Storm. Part III: Interaction of Inertial Currents and Mesoscale Eddies. *Journal of Physical Oceanography*, 25, 2953–2958.

D'Asaro, E. A., Eriksen, C. C., Levine, M. D., Niiler, P., Paulson, C. A., & Meurs, P. V. (1995). Upper-Ocean Inertial Currents Forced by a Strong Storm. Part I: Data and Comparisons with Linear Theory. *Journal of Physical Oceanography*, 25, 2909–2936.

Dohan, K. & Davis, R. E. (2011). Mixing in the transition layer during two storm events. *Journal of Physical Oceanography*, 41, 42–66. doi: 10.1175/2010JPO4253.1.

Elipot, S. & Lumpkin, R. (2008). Spectral description of oceanic near-surface variability. *Geophysical Research Letters*, 35(L05606), 1–5. doi: 10.1029/2007GL032874.

Elipot, S., Lumpkin, R., & Prieto, G. (2010). Modification of inertial oscillations by the mesoscale eddy field. *Journal of Geophysical Research*, 115(C09010), 1–20.

Garrett, C. (2001). What is the "Near-Inertial" Band and Why Is It Different from the Rest of the Internal Wave Spectrum? *Journal of Physical Oceanography*, 31, 962–971.

Hadley, M. (2010). Entrance Hall pendulum and display. http://www2.warwick.ac.uk/fac/sci/physics/pendulum/. [Accessed 13 August 2014].

Jochum, M., Briegleb, B. P., Danabasoglu, G., Large, W. G., Norton, N. J., Jayne, S., Alford, M. H., & Bryan, F. O. (2013). The Impact of Oceanic Near-Inertial Waves on Climate. *American Meteorological Society*, 26, 2833–2844. doi: 10.1175/JCLI-D-12-00181.1.

Kanasewich, E. R. (1981). *Time Sequence Analysis in Geophysics*. University of Alberta Press, third edition.

Kantha, L. H. & Clayson, C. A. (2000). *Numerical Models of Oceans and Oceanic Processes*, volume 66 of *International Geophysics Series*. Academic Press.

Knauss, J. A. (2005). *Introduction to Physical Oceanography*. Waveland Press, Inc., second edition.

Large, W. G. & Crawford, G. B. (1995). Observations and Simulations of Upper-Ocean Response to Wind Events during the Ocean Storms Experiment. *American Meteorological Society*, 25, 2831–2852.

Large, W. G., McWilliams, J. C., & Doney, S. C. (1994). Oceanic vertical mixing: A review and a model with a nonlocal boundary layer parameterization. *Reviews of Geophysics*, 34(4), 363–403.

Large, W. G., Morzel, J., & Crawford, G. B. (1995). Accounting for Surface Wave Distortion of the Marine Wind Profile in a Low-Level Ocean Storms Wind Measurements. *Journal of Physical Oceanography*, 25, 2959–2971.

Large, W. G. & Yeager, S. G. (2004). *Diurnal to Decadal Global Forcing For Ocean and Sea-Ice Models: The Data Sets and Flux Climatologies*. NCAR Technical Note NCAR/TN-460+STR, National Center for Atmospheric Research.

Large, W. G. & Yeager, S. G. (2009). The global climatology of an interannually varying air-sea flux data set. *Climate Dynamics*, 33, 341–364. doi: 10.1007/s00382-008-0441-3.

Levine, M. D. & Zervakis, V. (1995). Near-Inertial Wave Propagation into the Pycnocline during Ocean Storms: Observations and Model Comparison. *Journal of Physical Oceanography*, 25, 2890–2908.

Mellor, G. L. (1996). *Introduction to Physical Oceanography*. American Institute of Physics.

Niieler, P. P. & Paduan, J. D. (1995). Wind-driven Motions in the Northeast Pacific as Measured by Lagrangian Drifters. *Journal of Physical Oceanography*, 25, 2819–2830.

NOAA (webA). Prediction and Research Moored Array in the Atlantic (PIRATA). http://www.pmel.noaa.gov/pirata/. [Accessed 2 September 2014].

NOAA (webB). Mooring information. http://www.pmel.noaa.gov/tao/proj_over/mooring.shtml#standard. [Accessed 2 September 2014].

Plueddemann, A. J. & Farrar, J. T. (2006). Observations and models of the energy flux from the wind to Mixed-layer inertial currents. *Deep-Sea Research, part II*, 53, 5–30.

Price, J. F. (1981). Upper Ocean Response to a Hurricane. *Journal of Physical Oceanography*, 11, 153–175.

Qi, H., de Szoeke, R. A., Paulson, C. A., & Eriksen, C. C. (1995). The Structure of Near-Inertial Waves during Ocean Storms. *Journal of Physical Oceanography*, 25.

Riley, K. F., Hobson, M. P., & Bence, S. J. (2006). *Mathematical Methods for Physics and Engineering*. Cambridge University Press, third edition.

Rimac, A., von Storch, J., Eden, C., & Haak, H. (2013). The influence of high-resolution wind stress field on the power input to near-inertial motions in the ocean. *Geophysical Research Letters*, 40, 4882–4886. doi: 10.1002/grl.50929.

Servain, J., Busalacchi, A. J., McPhaden, M. J., Moura, A. D., Reverdin, G., Vianna, M., & Zebiak, S. E. (1998). A Pilot Moored Array in the Tropical Atlantic (PIRATA). *Bulletin of the American Meteorological Society*, 79(10), 2019–2031.

Stewart, R. H. (2008). *Introduction To Physical Oceanography*. Texas A & M University.

UCAR (webA). About CESM. http://www2.cesm.ucar.edu/about. [Accessed 21 November 2013].

Vallis, G. K. (2006). *Atmospheric and Oceanic Fluid Dynamics: Fundamentals and Large-Scale Circulation*. Cambridge University Press, first edition.

Wallace, J. M. & Hobbs, P. V. (2006). *Atmospheric Science: An introductory survey*. Elsevier, second edition.

Wallcraft, A. J., Metzger, E. J., & Carroll, S. N. (2009). *Software Design Description for the Hybrid Coordinate Ocean Model (HYCOM) Version 2.2*. Memorandum Report NRL/MR/7320–09-9166, Naval Research Laboratory, Ocean Division.

Zervakis, V. & Levine, M. D. (1995). Near-Inertial Energy Propagation from the Mixed Layer: Theoretical Considerations. *Journal of Physical Oceanography*, 25, 2872–2889.